Uniform asymptotic approximations for transient waves due to an initial disturbance

Madsen, Per A.; Schäffer, Hemming A.; Fuhrman, David R.; Toledo, Yaron

Published in:
Journal of Geophysical Research: Oceans

Link to article, DOI:
10.1002/2015jc011155

Publication date:
2016

Document Version
Peer reviewed version

Research Article

Journal of Geophysical Research: Oceans
DOI 10.1002/2015JC011155

Uniform asymptotic approximations for transient waves due to an initial disturbance

Per A. Madsen[1], Hemming A. Schäffer[2], David R. Fuhrman[1] and Yaron Toledo[3]

1: Department of Mechanical Engineering, Technical University of Denmark, DK-2800, Kgs Lyngby, Denmark.

2: SchäfferWaves, Sortedam Dossering 59D ST, DK-2100, Copenhagen Ø, Denmark

3: School of Mechanical Engineering, Faculty of Engineering, Tel Aviv University, Israel.

P.A. Madsen, Department of Mechanical Engineering, Technical University of Denmark, Nils Koppels All, building 403, 2800 Kgs Lyngby, Denmark. (prmr@mek.dtu.dk)

Received: Jul 23, 2015; Revised: Nov 02, 2015; Accepted: Nov 26, 2015

Abstract. In this work, we first present a semi-analytical method for the evolution of linear fully-dispersive transient waves generated by an initial surface displacement and propagating over a constant depth. The procedure starts from Fourier and Hankel transforms and involves a combination of the method of stationary phase, the method of uniform asymptotic approximations and various Airy integral formulations. Secondly, we develop efficient convolution techniques expressed as single and double summations over the source area. These formulations are flexible, extremely fast and highly accurate even for the dispersive tail of the transient waves. To verify the accuracy of the embedded dispersion properties, we consider test cases with sharp-edged disturbances in 1D and 2D. Furthermore, we consider the case of a relatively blunt Gaussian disturbance in 2D. In all cases the agreement between the convolution results and simulations with a high-order Boussinesq model is outstanding.

Finally, we make an attempt to extend the convolution methods to geophysical tsunami problems taking into account e.g. uneven bottom effects. Unfortunately, refraction/diffraction effects cannot easily be incorporated, so instead we focus on the incorporation of linear shoaling and its effect on travel time and temporal evolution of the surface elevation. The procedure is tested on data from the 2011 Japan tsunami. Convolution results are likewise compared to model simulations based on the nonlinear shallow water equations and both are compared with field observations from 10 deep wa-

ter DART buoys. The near-field results are generally satisfactory, while the far-field results leave much to be desired.

1. Introduction

Tsunamis generated by seismic activity in the deep ocean are typically transient wave trains propagating large distances over almost constant depth. During this propagation nonlinearity is relatively small and the wave train can be assumed to be linear. The front of the wave train moves approximately with the linear shallow water celerity, while the leading wave is influenced by weak dispersion. Behind the leading wave, a tail with more dispersive waves will appear and dispersion will gradually become more and more important with the distance from the leading wave. The significance of the tail depends on the spatial gradients of the initial disturbance: Very sharp disturbances will immediately generate strong tails with highly dispersive waves, while blunt disturbances will produce only a single leading wave. During the propagation over large distances, however, transient waves will evolve under the accumulated influence of dispersion, leading to a gradual change of representative wave periods and a stronger and stronger dispersive tail.

Weak dispersion can typically be handled by any standard Boussinesq model and these are now being used for tsunami modelling on a regular basis (see e.g. Løvholt et al. 2012; Glimsdal et al. 2013; Grilli et al. 2013). It is, however, still common to use models based on the non-dispersive nonlinear shallow water (NSW) equations (see e.g. Tang et al. 2012; Ren et al. 2013). In principle, the NSW equations cannot correctly predict the temporal evolution of the transient waves, but it has to be admitted that these models have been relatively successful in simulating geophysical tsunamis.

In this work, we shall focus on transient linear dispersive water waves, induced by an initial localized disturbance and propating over a constant depth. Our goal is to develop

a fast, flexible and accurate semi-analytical model for the evolution of these waves and to incorporate full dispersion in this process. Fundamentally, this corresponds to the classical Cauchy-Poisson problem, which has been described by e.g. Lamb (1932), Wehausen & Laitone (1960) and LeBlond & Mysak (1978). First of all, the surface elevation can be expressed by integral transforms relating the fluid motion at time t and position x to the prescribed initial disturbance. Secondly, these transforms can be approximated by asymptotic expansions valid for relatively large values of time and space from the disturbance. Classical solutions to this problem can be found in e.g. Kajiura (1963), Whitham (1974) and Newman (1991). These solutions typically describe the evolution of the leading wave near the wave front (in which case weak dispersion can be assumed) or the trailing waves far behind the wave front, in which case the method of stationary phase can be utilized. The classical solutions are non-uniform as they cannot describe the complete range of wave numbers present in the wave train.

Clarisse, Newman and Ursell (1995) were the first to develop *uniform* asymptotic solutions to the Cauchy-Poisson problem in both one and two-dimensions, which implies that these solutions were uniformly valid for the complete interval of wave numbers (i.e. from weak dispersion to full dispersion). This was a remarkable achievement, but unfortunately their work has attracted very little attention. Today, 20 years later their publication has obtained only six references according to Web of Science (e.g. Kuznetsov, 2006; Ursell, 2007; Sekerzh-Zenkovich, 2009; Glimsdal et al., 2007 & 2013), none of which have actually utilized the findings of the original paper. Several reasons for this lack of attention could be suggested: First, the paper was very condensed and the method rather cumbersome. Second, no applications were presented leaving the full potential of the theory

implied, rather than directly demonstrated. More recently, Berry (2005) presented a similar, but more elegant, derivation without being aware of the original work by Clarisse et al. (1995). Berry provided a few applications but they were limited to idealized narrow Gaussian disturbances.

Our first objective in the present paper is to re-derive and discuss the classical as well as the uniform asymptotic theory with the proper links to Whitham (1974), Clarisse et al. (1995) and Berry (2005). In this connection, we start from the classical integral formulations in terms of Fourier and Hankel transforms, and utilize a combination of the method of stationary phase, the method of uniform asymptotic approximations and various Airy integral formulations to obtain efficient but accurate impulse response functions. Section 2 covers the case of an initial 1D surface elevation, while section 3 covers the case of an initial 2D radially symmetric surface elevation. Section 4 covers the variables of uniform approximations and discusses their variation behind, near and beyond the front of the wave train.

Our second objective is to extend the uniform asymptotic theory beyond the achievements of Clarisse et al. and Berry by developing efficient convolution procedures in 1D and 2D in order to solve problems with general configurations of the initial disturbance. To this end, Section 5 introduces efficient convolution techniques to be used for problems on a constant depth, while Section 6 presents a number of test examples where the 1D and 2D approximations are applied and verified. This includes an initial 1D rectangular disturbance, an initial 2D square disturbance, and an initial 2D Gaussian disturbance. The convolution solutions are compared with numerical results from models solving lin-

ear high-order Boussinesq equations (Madsen et al., 2002) as well as linear shallow water equations (Ren et al., 2013).

Our third objective is to investigate a possible extension of the asymptotic theories and their convolution methods to geophysical problems with uneven bottom. This has not been attempted previously in the literature, and success is by no means guaranteed. Ideally, this requires that shoaling, refraction and diffraction are incorporated and furthermore it involves special effects related to the motion on a sphere. Unfortunately, diffraction and refraction effects are not readily incorporated in the present model, and we have chosen to focus on the incorporation of linear shoaling and its influence on the travel time of the leading wave. These effects are approximated by using linear shallow water theory, which is justified by the fact that natural tsunami sources often appear with relatively mild spatial gradients. Section 7 covers the extension to uneven bottom and a special convolution procedure suited for this purpose. As a test example, we focus on the 2011 Tohoku tsunami, and compare the convolution results with DART measurements and with numerical results obtained from solving the nonlinear shallow water equations (Ren et al., 2013).

2. The response to an initial 1D disturbance of the free surface

2.1. Introduction

We consider the classical problem of linear water waves generated by an initial disturbance of the free surface. A Cartesian coordinate system is adopted with the x-axis located at the *still water level* (SWL) and with the z-axis pointing vertically upwards. Hence, the fluid domain is bounded by the horizontal sea bed at $z = -h$ and by the free surface $z = \eta(x, t)$. Expressions will be derived in terms of non-dimensional variables

where horizontal (x) and vertical (z and η) distances are scaled with the water depth h i.e.

$$X \equiv \frac{x}{h}, \quad Z \equiv \frac{z}{h}, \quad \zeta \equiv \frac{\eta}{h}, \tag{1}$$

while time (t), cyclic frequency (ω) and the wave number (k) are non-dimensionalized as

$$\tau \equiv t\sqrt{\frac{g}{h}}, \qquad \Omega \equiv \omega\sqrt{\frac{h}{g}}, \qquad \kappa \equiv kh, \tag{2}$$

where g is the acceleration of gravity. The linear dispersion relation for the wave propagation generally reads

$$\Omega^2 = \kappa \tanh \kappa,$$

with the associated relevant expression for $\Omega[\kappa]$ being

$$\Omega[\kappa] = \text{sign}[\kappa]\sqrt{\kappa \tanh \kappa}. \tag{3}$$

2.2. General formulation based on Fourier integrals

The initial one-dimensional disturbance of the free surface is described by

$$\zeta[X, 0] \equiv F[X], \quad \text{and} \quad \zeta_\tau[X, 0] = 0, \tag{4}$$

where $F[X]$ defines the arbitrary shape of this disturbance. As described by e.g. Whitham (1974, §13.5), the response to this disturbance is determined by

$$\zeta_1[X,\tau] = \int_{-\infty}^{\infty} \Gamma_1[\kappa](\exp[i(\kappa X - \Omega\tau)] + \exp[i(\kappa X + \Omega\tau)])d\kappa, \tag{5}$$

where $\Gamma_1[\kappa]$ is the Fourier transform of the initial condition i.e.

$$\Gamma_1[\kappa] = \frac{1}{4\pi}\int_{-\infty}^{\infty} F[X]\exp[-i\kappa X]dX. \tag{6}$$

For the special case of $F[X] = \delta[X]$, i.e. a 1D Dirac delta-function disturbance, $\zeta_1[X,\tau]$ becomes the impulse-response function, while (6) yields

$$\Gamma_{1\delta}[\kappa] = \frac{1}{4\pi}. \tag{7}$$

In the following, we consider the asymptotic behaviour of the solution for $\tau \to \infty$ and $X/\tau > 0$. This implies that the backward going waves can be ignored and (5) simplifies to

$$\zeta_2[X,\tau] = \int_{-\infty}^{\infty} \Gamma_1[\kappa]\exp[-i\tau\Phi]d\kappa, \tag{8}$$

where

$$\Phi \equiv \Omega[\kappa] - \kappa a, \qquad \text{and} \qquad a \equiv \frac{X}{\tau}. \tag{9}$$

Note that according to (1)-(2), we have that $a = x/(t\sqrt{gh})$. Hence, the front of the wave train, which moves with the non-dispersive shallow water celerity, corresponds to $a \to 1$, while the dispersive tail of the transient wave corresponds to lower values of a.

2.3. The method of stationary phase for oscillating integrals

The method of stationary phase was first discussed by Stokes (1850) and Lord Kelvin (see Thomson, 1887) and since then it has been used in many contexts in the literature. Good reviews of the method can be found in e.g. Whitham (1974) and Wong (1989).

The objective is to approximate oscillating integrals of the type (8) for large values of τ. In this case $\Gamma_1[\kappa]$ will typically be slowly varying, while the phase $\tau\Phi$ will oscillate rapidly with κ. This generally leads to cancelations in the integral unless there are points κ_i where the phase is stationary. These stationary points are defined by

$$\frac{d\Phi}{d\kappa}[\kappa_i] = 0. \tag{10}$$

For the present case, the principal contribution to (8) comes from the two stationary points $\kappa = \pm\kappa_0$, where κ_0 satisfies

$$\frac{d\Phi}{d\kappa} = \Omega_\kappa[\kappa_0] - a = 0, \qquad \text{where} \qquad \Omega_\kappa \equiv \frac{d\Omega}{d\kappa}. \tag{11}$$

We note that Ω_κ represents the local group velocity of the wave train.

Whitham (1974, §11.3) and Kajiura (1963) used the method of stationary phase on (8) to derive the classical asymptotic approximation

$$\zeta_3[X,\tau] = 2\Gamma_1[\kappa_0]\sqrt{\frac{2\pi}{-\tau\Omega_{\kappa,\kappa}}}\cos\left[-\tau\Phi[\kappa_0] + \frac{\pi}{4}\right], \tag{12}$$

where $\Omega_{\kappa,\kappa}$ denotes the second derivative of Ω with respect to κ.

2.4. The weakly dispersive solution valid near the front of the wave train

Whitham (1974, §13.6) and Kajiura (1963) analysed the conditions near the front of the wave train, where dispersion collapses and the waves become shallow water waves with $\kappa \to 0$. A brief summary of this derivation follows. First of all, a Taylor expansion about $\kappa = 0$ of the linear dispersion relation leads to the KdV (Korteweg-de Vries) approximation

$$\Omega \simeq \kappa - \frac{1}{6}\kappa^3, \qquad \Rightarrow \qquad \Phi \simeq (1-a)\kappa - \frac{1}{6}\kappa^3, \tag{13}$$

and in this case (8) simplifies to

$$\zeta_4[X,\tau] = \Gamma_1[0] \int_{-\infty}^{\infty} \exp\left[i\kappa(X-\tau) + \frac{1}{6}i\kappa^3\tau\right] d\kappa. \tag{14}$$

At this point, it is useful to consider the definition of the Airy function

$$Ai[s] \equiv \frac{1}{\pi}\int_0^{\infty} \cos\left[sw + \frac{1}{3}w^3\right] dw = \frac{1}{2\pi}\int_{-\infty}^{\infty} \exp\left[i\left(sw + \frac{1}{3}w^3\right)\right] dw, \tag{15}$$

see e.g. Vallée & Soares (2004). Hence, a comparison between (15) and (14) suggests the transformations

$$\frac{1}{3}w^3 = \frac{1}{6}\tau\kappa^3 \qquad \Rightarrow \qquad \kappa = w\left(\frac{2}{\tau}\right)^{1/3}, \tag{16}$$

$$sw = \kappa(X-\tau) \qquad \Rightarrow \qquad s = (X-\tau)\left(\frac{2}{\tau}\right)^{1/3} = -(1-a)2^{1/3}\tau^{2/3}. \tag{17}$$

This implies that (14) can be expressed as

$$\zeta_4[X,\tau] = 2\pi\Gamma_1[0]\left(\frac{2}{\tau}\right)^{1/3} Ai\left[-(1-a)2^{1/3}\tau^{2/3}\right]. \tag{18}$$

Figure 1 shows the spatial variation of the 1D surface elevation as a function of $a = X/\tau$ at time $\tau = 100$ for the special case of an initial delta-function disturbance. We note that ζ_3 given by (12) has a singularity near the front of the wave train where $a \to 1$ and $\Omega_{\kappa,\kappa} \to 0$. This problem is resolved by ζ_4 which describes the transition from the oscillatory motion behind the front ($a < 1$) to the exponentially decaying motion beyond the front ($a > 1$). However, it is clear that the KdV dispersion relation imbedded in ζ_4 quickly becomes inadequate and the solution starts to deviate significantly from ζ_3 in phase as well as in amplitude for smaller values of a.

2.5. Uniform asymptotic approximations in 1D

The main objective of the so-called *uniform* asymptotic approximations is to transform the integrand of oscillating integrals such as (8) into a simpler form allowing an analytical evaluation of the integral with the solution being uniformly valid for the complete interval of wave numbers (i.e. from weak dispersion to full dispersion). In contrast to the non-uniform procedures described in the previous section (and applied by e.g. Kajiura, 1963 and Whitham, 1974), the uniform procedure retains full dispersion by mapping the variables of integration into a new set of variables while stretching the validity via the method of stationary phase. The general concept of uniform asymptotic transformations of oscillating integrals goes back to Chester et al. (1957), Ursell (1965), Bleistein (1966, 1967), Child (1975) and Ursell (1980). More recent discussions of the technique can be found in Wong (1989), Vallée & Soares (2004) and Ursell (2007). Clarisse et al. (1995) were the first to apply this method on the Cauchy-Poisson problem and their method for the 1D problem will be summarized in the following.

In the frame work of Airy type solutions, Φ should be expressed as a cubic function. In this connection, Clarisse et al. (1995) used the form

$$\Phi[u] = \varepsilon u - \frac{1}{6}u^3, \tag{19}$$

while Berry (2005) used the form

$$\Phi[v] = -\sigma v - \frac{1}{3}v^3, \tag{20}$$

where u and v are new integration variables (replacing κ), while ε and σ are functions to be determined from matching conditions. Choosing (19) or (20) as the starting point is not important, and throughout this work we have chosen the (u, ε) formulation (19).

In the following, we shall now consider κ to be a function of u, and consequently (9) can be expressed as

$$\Phi[u] \equiv \Omega[\kappa[u]] - \kappa[u]a. \tag{21}$$

The matching of (19) and (21) now implicitly defines the new variable u.

On the basis of the transformation (19), we can replace (8) by

$$\zeta_5[X,\tau] = \int_{-\infty}^{\infty} \Gamma_1[\kappa[u]] G_1[u] \exp\left[i\tau\left(-\varepsilon u + \frac{1}{6}u^3\right)\right] du, \tag{22}$$

where

$$G_1[u] \equiv \frac{d\kappa}{du}. \tag{23}$$

The next step is to assume that Γ_1 and G_1 are slowly varying functions of u and to apply the method of stationary phase, by which the integral in (22) can be approximated by

$$\zeta_6[X,\tau] = \Gamma_1[\kappa_0]G_1[u_0]\int_{-\infty}^{\infty} \exp\left[i\tau\left(-\varepsilon u + \frac{1}{6}u^3\right)\right] du, \tag{24}$$

where u_0 defines the value of u at the first stationary point. A comparison with the definition of the Airy function (15) now suggests the transformations

$$\frac{1}{3}w^3 = \frac{\tau}{6}u^3 \qquad \Rightarrow \qquad u = w\left(\frac{2}{\tau}\right)^{1/3}, \tag{25}$$

$$sw = -\tau\varepsilon u \qquad \Rightarrow \qquad s = -\varepsilon 2^{1/3}\tau^{2/3}. \tag{26}$$

This implies that (24) can be expressed as

$$\zeta_6[X,\tau] = 2\pi\Gamma_1[\kappa_0]G_1[u_0]\left(\frac{2}{\tau}\right)^{1/3} Ai\left[-\varepsilon 2^{1/3}\tau^{2/3}\right], \tag{27}$$

where Γ_1 and G_1 are defined by (6) and (23), respectively. The determination of κ_0, u_0, ε and $G_1[u_0]$ and the accuracy of (27) will be pursued in section 4.

3. The response to an initial 2D disturbance of the free surface

3.1. A radially symmetric disturbance of the free surface

The linearized problem of an initial radially symmetric disturbance of the free surface was treated by e.g. Wehausen & Laitone (1960), Whitham (1974), and LeBlond & Mysak (1978). The initial disturbance is assumed to vary only with the radial distance $R \equiv r/h$ and have no angular dependence i.e.

$$\zeta[R,0] \equiv F[R], \quad \text{and} \qquad \zeta_\tau[R,0] = 0. \tag{28}$$

As described by Whitham (1974, §13.5), the surface elevation generated by this disturbance can be determined by

$$\zeta_{11}[R,\tau] = \int_0^\infty \Gamma_2[\kappa] J_0[\kappa R] \cos[\Omega\tau] \kappa d\kappa, \tag{29}$$

where Γ_2 is the Hankel transform defined by

$$\Gamma_2[\kappa] = \int_0^\infty F[R] J_0[\kappa R] R dR. \tag{30}$$

For the special case of a delta-function located at the origin, $F[R]$ is defined by

$$F[R] = \frac{\delta[R]}{2\pi R}. \tag{31}$$

In this case $\zeta_{11}[X,\tau]$ becomes the impulse-response function, and (30) leads to

$$\Gamma_{2\delta}[\kappa] = \frac{1}{2\pi}. \tag{32}$$

3.2. Uniform asymptotic approximations in 2D

On the basis of the work by Chester et al. (1957), Ursell (1965), Bleistein (1966, 1967) and Ursell (1980), Clarisse et al. (1995) were the first to derive a 2D uniform asymptotic approximation to (29) combined with (31). As a first step, they extended the integration from $-\infty$ to ∞, while replacing the Bessel function J_0 with the Hankel function $H_0^{(2)}$ of the second kind. Second, they replaced the Hankel function by its integral representation leading to the double integral

$$\zeta_{12}[R,\tau] = \frac{i 2^{-3/2}}{2\pi^2} \int_{-\infty}^{\infty}\int_{-\infty}^{\infty} \kappa \left(1 + \frac{1}{2}\sigma^2\right)^{-1/2} \exp[i\tau\Psi] d\kappa d\sigma,$$

with

$$\Psi \equiv \Omega[\kappa] - \kappa\left(1+\sigma^2\right)a, \qquad \text{and} \qquad a \equiv \frac{R}{\tau}.$$

Third, the integration variables (κ, σ) were replaced by the stretched variables (u, v) defined by the two relations

$$\varepsilon u - \frac{1}{6}u^3 = \Omega[\kappa] - \kappa a, \quad \text{and} \qquad uv^2 = \kappa\sigma^2.$$

Fourth, these variables were replaced by a new set of stretched variables (ξ, λ) defined by

$$u = \alpha(\xi + \lambda), \qquad \text{and} \quad v = \beta(\xi - \lambda).$$

With these transformations, the method of stationary phase resulted in four saddle points for $(\xi_0^{\pm}, \lambda_0^{\pm})$ and after cumbersome algebraic manipulations the surface elevation was finally expressed in terms of the product of the Airy function and its derivative.

More recently, Berry (2005) considered the same problem, apparently being unaware of the original work by Clarisse et al. (1995). However, Berry pursued a much more direct and straight forward path, which we summarize in the following. First of all, the Bessel function J_0 is expressed by its integral definition

$$J_0[\kappa R] \equiv \frac{1}{2\pi}\int_0^{2\pi} \exp[i\kappa R\cos\theta]d\theta. \tag{33}$$

Secondly, the method of stationary phase is applied to (33) leading to the two stationary points $\theta_1 = 0$ and $\theta_2 = \pi$. Now a Taylor expansion about each of these points leads to

$$\cos\theta \simeq 1 - \frac{1}{2}\theta^2, \qquad \text{for } \theta \simeq \theta_1,$$
$$\cos\theta \simeq -1 + \frac{1}{2}(\theta - \pi)^2, \qquad \text{for } \theta \simeq \theta_2,$$

by which the integration in (33) can be analytically executed near each stationary point. This leads to

$$\begin{aligned} J_0[\kappa R] &\simeq \frac{1}{2\pi}\left(\sqrt{\frac{\pi}{\kappa R}}(1-i)\exp[i\kappa R] + \sqrt{\frac{\pi}{\kappa R}}(1+i)\exp[-i\kappa R]\right) \\ &= \sqrt{\frac{2}{\pi\kappa R}}\cos\left[\kappa R - \frac{\pi}{4}\right]. \end{aligned} \tag{34}$$

We note that (34) is the classical asymptotic approximation for J_0 valid for large values of κR.

Next, (34) is inserted in (29) and as a result the integrand contains two terms, representing waves propagating away from and towards the source, respectively. The latter is ignored by which we obtain the following asymptotic approximation to (29)

$$\zeta_{13}[R,\tau] = \int_0^\infty \frac{\Gamma_2[\kappa]\kappa^{1/2}}{(2\pi R)^{1/2}}\cos\left[\tau\Phi + \frac{\pi}{4}\right] d\kappa, \tag{35}$$

where

$$\Phi[\kappa] \equiv \Omega[\kappa] - \kappa a, \qquad a \equiv \frac{R}{\tau}. \tag{36}$$

The next step is to introduce the uniform transformation of variables exactly as in 1D i.e. κ is replaced by u defined by (19). In this process the following connection is utilized

$$\kappa^{1/2} d\kappa = G_2 u^{1/2} du, \tag{37}$$

where

$$G_2 \equiv \frac{d\kappa}{du}\sqrt{\frac{\kappa}{u}}. \tag{38}$$

The functions G_2 and Γ_2 are assumed to be slowly varying with u and are therefore estimated by their values at the stationary phase points $u = \pm u_0$. On this basis, the integral (35) transforms into

$$\zeta_{14}[R,\tau] = \frac{\Gamma_2[u_0]G_2[u_0]}{(2\pi R)^{1/2}} \int_0^\infty \cos\left[\tau\left(\varepsilon u - \frac{1}{6}u^3\right) + \frac{\pi}{4}\right] u^{1/2} du. \tag{39}$$

It turns out that this integral can be expressed in terms of Airy functions. Berry (2005) provided the result in his equation (5.5), but omitted the derivation, which is given here, as we do not find it completely trivial. The starting point is to consider the following integral definition of the product of the Airy function and its derivative

$$Ai[s]Ai'[s] \equiv \left(\frac{1}{2\pi}\right)^2 \int_{-\infty}^{\infty}\int_{-\infty}^{\infty} iv \exp\left[i\left((v+w)\,s + \frac{1}{3}\left(v^3+w^3\right)\right)\right] dvdw. \tag{40}$$

Next, we introduce a coordinate transformation from (v, w)-variables to (ξ, λ)-variables defined by

$$w = \beta(\xi+\lambda), \quad \text{and} \quad v = \beta(\xi-\lambda). \tag{41}$$

The absolute value of the corresponding Jacobian determinant is $2\beta^2$. With this coordinate transformation it is now possible to analytically integrate the λ-integral and as a result (40) simplifies to

$$Ai[s]Ai'[s] = -\frac{1}{2^{1/2}\pi^{3/2}}\int_0^\infty \cos\left[-2\xi\beta s - \frac{2}{3}\xi^3\beta^3 + \frac{\pi}{4}\right]\beta^{3/2}\xi^{1/2}d\xi. \tag{42}$$

The matching of (42) and (39) now yields

$$u = \frac{2}{\tau^{1/2}}\xi, \quad s = -\frac{\varepsilon\tau^{2/3}}{2^{1/3}}, \quad \beta = \frac{2^{1/3}}{\tau^{1/6}},$$

and as a result the asymptotic surface elevation can be determined by

$$\zeta_{15}[R,\tau] = -\frac{2\pi\Gamma_2[\kappa_0]G_2[u_0]}{\sqrt{R\tau}}Ai\left[-\varepsilon 2^{-1/3}\tau^{2/3}\right]Ai'[-\varepsilon 2^{-1/3}\tau^{2/3}], \tag{43}$$

where Γ_2 and G_2 are defined by (30) and (38), respectively. The determination of κ_0, u_0, ε, $G_1[u_0]$ and $G_2[u_0]$ will be pursued in section 4.

4. The governing parameters in the uniform asymptotic approximations

Before we can utilize the uniform asymptotic approximations given in (27) for 1D and (43) for 2D, we need to determine κ_0, u_0, ε, $G_1[u_0]$ and $G_2[u_0]$ at the stationary points. The following derivation is split in three parts: First, we concentrate on conditions behind the wave front i.e. for $0 < a < 1$. Second, we focus on conditions ahead of the front i.e. for $a > 1$. Third, we present Taylor expansions for $a \to 1$. These expressions will bridge the formulations behind and ahead of the front, and in addition they will provide practical approximations to the general expressions.

4.1. Solutions for $0 < a < 1$

In order to determine $\kappa = \kappa_0$, we first differentiate the dispersion relation (3) with respect to κ and obtain

$$\Omega_\kappa = \text{sign}[\kappa] \left(\frac{\kappa \,\text{sech}^2\, \kappa + \tanh \kappa}{2\sqrt{\kappa \tanh \kappa}} \right). \tag{44}$$

This is an even function of κ i.e. $\Omega_\kappa[-\kappa] = \Omega_\kappa[\kappa]$ and for this reason (11) will be satisfied by κ_0 as well as by $-\kappa_0$. We assume that $\kappa_0 > 0$, and insert (44) in (11), which leads to the condition

$$\frac{\kappa_0 \,\text{sech}^2\, \kappa_0 + \tanh \kappa_0}{2\sqrt{\kappa_0 \tanh \kappa_0}} = a, \qquad \text{for} \quad \kappa_0 > 0. \tag{45}$$

For $0 < a < 1$, (45) will provide real number solutions for κ_0, which will obviously be a function of a.

Next, let us determine the value of $u = u_0$ at the first stationary point $\kappa = \kappa_0$. First, we differentiate (19) with respect to u to obtain

$$\frac{d\Phi}{du} = \varepsilon - \frac{1}{2}u^2. \tag{46}$$

Second, we differentiate (21) with respect to u to obtain

$$\frac{d\Phi}{du} = \frac{d\kappa}{du}\left(\Omega_\kappa - a\right). \tag{47}$$

According to (11), it is clear that (47) will be zero at the first stationary point, and consequently (46) also needs to be zero. This leads to the matching condition

$$\varepsilon = \frac{1}{2}u_0^2. \tag{48}$$

Third, (19) and (21) obviously need to match for all values of u and therefore also at the first stationary point $u = u_0$. According to (48), this leads to

$$\Phi[u_0] = \frac{1}{3}u_0^3, \quad \text{and} \quad \Phi[u_0] = \Omega[\kappa_0] - \kappa_0 a, \tag{49}$$

by which we obtain

$$u_0 = 3^{1/3}\left(\Omega[\kappa_0] - \kappa_0 a\right)^{1/3}, \tag{50}$$

$$\varepsilon = \frac{1}{2}3^{2/3}\left(\Omega[\kappa_0] - \kappa_0 a\right)^{2/3}. \tag{51}$$

With κ_0 being a function of a, we note that also u_0 and ε are functions of a.

Fourth, we need to evaluate $G_1[u]$ defined by (23). By matching (46) and (47) we obtain the general expression

$$G_1[u] \equiv \frac{d\kappa}{du} = \left(\frac{\varepsilon - \frac{1}{2}u^2}{\Omega_\kappa - a}\right). \tag{52}$$

Towards the first stationary point, the numerator as well as the denominator of (52) go to zero. Consequently, we need to Taylor-expand the numerator as well as the denominator with respect to u in the vicinity of u_0 until we get non-zero contributions. Thus, by applying L'Hôspital's rule on (52) we obtain

$$\Omega_{\kappa,\kappa}\left(\frac{d\kappa}{du}\right)^2 = -u, \qquad \text{for } u = u_0,$$

which leads to the result

$$G_1[u_0] \equiv \frac{d\kappa}{du}[u_0] = \sqrt{\frac{u_0}{-\Omega_{\kappa,\kappa}[\kappa_0]}}. \tag{53}$$

Note that u_0 is given by (50), while $\Omega_{\kappa,\kappa}$ can be determined by differentiating (44) with the result

$$\Omega_{\kappa,\kappa}[\kappa] = \mathrm{sign}[\kappa]\left(\frac{-1+3\kappa^2\,\mathrm{sech}^4\,\kappa+\mathrm{sech}^2\,\kappa\,(1-4\kappa^2+2\kappa\tanh\kappa)}{4\,(\kappa\tanh\kappa)^{3/2}}\right). \tag{54}$$

We note that $\Omega_{\kappa,\kappa}$ is an odd function of κ i.e. that $\Omega_{\kappa,\kappa}[-\kappa] = -\Omega_{\kappa,\kappa}[\kappa]$.

Finally, we need to evaluate $G_2[u]$ defined by (38). By inserting (53) we obtain

$$G_2[u_0] \equiv \sqrt{\frac{\kappa_0}{u_0}}\frac{d\kappa}{du}[u_0] = \sqrt{\frac{\kappa_0}{-\Omega_{\kappa,\kappa}[\kappa_0]}}. \tag{55}$$

4.2. Taylor expansions for $a \to 1$

Near the front of the wave train we have that $a \to 1$ and $\kappa_0 \to 0$, hence we introduce the small parameter $\mu \equiv 1-a$. To obtain a Taylor expansion of κ_0 in terms of μ, we first expand (45) in terms of κ_0^2, then use successive approximations to invert this series as κ_0^2 in terms of μ and finally we expand the square root of this series to obtain

$$\kappa_0 = \sqrt{2\mu}\left(1+\frac{19}{36}\mu+\frac{1207}{2592}\mu^2+\frac{2588183}{5443200}\mu^3+....\right) \quad \text{for } \mu \to 0. \tag{56}$$

Next, we Taylor-expand u_0 and ε from (50) and (51) with respect to κ_0 and substitute (56) into the result. This leads to

$$u_0 = \sqrt{2\mu}\left(1+\frac{19}{180}\mu+\frac{25121}{453600}\mu^2+\frac{1996219}{48988800}\mu^3+....\right) \quad \text{for } \mu \to 0, \tag{57}$$

$$\varepsilon = \mu\left(1+\frac{19}{90}\mu+\frac{64}{525}\mu^2+\frac{178328}{1913625}\mu^3+....\right) \quad \text{for } \mu \to 0. \tag{58}$$

Finally, we Taylor expand $G_1[u_0]$ and $G_2[u_0]$ with respect to κ_0 by inserting (50) and (54) into (53) and (55). By substituting (56) into the result we obtain

$$G_1[u_0] \to \left(1 + \frac{38}{45}\mu + \frac{521}{567}\mu^2 + \frac{411574}{382725}\mu^3 + ...\right) \quad \text{for } \mu \to 0. \tag{59}$$

$$G_2[u_0] \to \left(1 + \frac{19}{18}\mu + \frac{815}{648}\mu^2 + \frac{1059679}{680400}\mu^3 + ...\right), \quad \text{for } \mu \to 0. \tag{60}$$

4.3. Solutions for $a > 1$

In order to extend the formulation to the region ahead of the front, we first need to find solutions to

$$\Omega_\kappa[\kappa_0] = a, \qquad \text{for} \quad a > 1. \tag{61}$$

This requires that κ_0 falls on the imaginary axis, hence we introduce

$$\kappa_0 = i\widetilde{\kappa}_0, \quad \text{and} \quad u_0 = i\widetilde{u}_0, \tag{62}$$

where the *tilde* indicates real number variables. According to (3), (44) and (54) this leads to

$$\Omega[i\widetilde{\kappa}_0] = i\sqrt{\widetilde{\kappa}_0 \tan\widetilde{\kappa}_0}, \tag{63}$$

$$\Omega_\kappa[i\widetilde{\kappa}_0] = \frac{\widetilde{\kappa}_0 \sec^2\widetilde{\kappa}_0 + \tan\widetilde{\kappa}_0}{2\sqrt{\widetilde{\kappa}_0 \tan\widetilde{\kappa}_0}}, \tag{64}$$

$$\Omega_{\kappa,\kappa}[i\widetilde{\kappa}_0] = i\left(\frac{-1 - 3\widetilde{\kappa}_0^2 \sec^4\widetilde{\kappa}_0 + \sec^2\widetilde{\kappa}_0\,(1 + 4\widetilde{\kappa}_0^2 - 2\widetilde{\kappa}_0 \tan\widetilde{\kappa}_0)}{4\,(\widetilde{\kappa}_0 \tan\widetilde{\kappa}_0)^{3/2}}\right). \tag{65}$$

This implies that $\widetilde{\kappa}_0$ is found as the solution to

$$\frac{\widetilde{\kappa}_0 \sec^2\widetilde{\kappa}_0 + \tan\widetilde{\kappa}_0}{2\sqrt{\widetilde{\kappa}_0 \tan\widetilde{\kappa}_0}} = a, \quad \text{for} \quad a > 1. \tag{66}$$

Next, we determine $\widetilde{u}_0$ and ε by inserting (62) and (63) into (49) and (48). This leads to

$$\widetilde{u}_0 = 3^{1/3}\left(\widetilde{\kappa}_0 a - \sqrt{\widetilde{\kappa}_0 \tan\widetilde{\kappa}_0}\right)^{1/3}, \qquad \text{for} \quad a > 1, \tag{67}$$

$$\varepsilon = -\frac{1}{2}3^{2/3}\left(\widetilde{\kappa}_0 a - \sqrt{\widetilde{\kappa}_0 \tan\widetilde{\kappa}_0}\right)^{2/3}, \qquad \text{for} \quad a > 1. \tag{68}$$

Note that in contrast to κ_0 and u_0, the continuation of ε from behind the front to ahead of the front actually takes place in the real domain.

Finally, we insert (62) and (65) into (53) and (55) and obtain

$$G_1[u_0] = \sqrt{\frac{\widetilde{u}_0}{-\widetilde{\Omega}_{\kappa,\kappa}[\widetilde{\kappa}_0]}}, \qquad \text{and} \qquad G_2[u_0] = \sqrt{\frac{\widetilde{\kappa}_0}{-\widetilde{\Omega}_{\kappa,\kappa}[\widetilde{\kappa}_0]}}, \qquad \text{for} \quad a > 1. \tag{69}$$

We note that G_1 and G_2 fall on the real axis also for $a > 1$.

4.4. The resulting surface elevations in 1D and 2D

Having determined $G_1[u_0]$ and $G_2[u_0]$, we can now insert (53) and (55) into (27) and (43) to obtain the 1D surface elevation

$$\zeta_7[X,\tau] = 2\pi\Gamma_1[\kappa_0]\sqrt{\frac{u_0}{-\Omega_{\kappa,\kappa}[\kappa_0]}}\left(\frac{2}{\tau}\right)^{1/3} Ai\left[-\varepsilon 2^{1/3}\tau^{2/3}\right], \tag{70}$$

and the 2D surface elevation

$$\zeta_{16}[R,\tau] = -\frac{2\pi\Gamma_2[\kappa_0]}{\sqrt{R\tau}}\sqrt{\frac{\kappa_0}{-\Omega_{\kappa,\kappa}[\kappa_0]}}Ai\left[-\varepsilon 2^{-1/3}\tau^{2/3}\right]Ai'[-\varepsilon 2^{-1/3}\tau^{2/3}]. \tag{71}$$

We note that Γ_1 and Γ_2 are defined by (6) and (30), while κ_0, u_0 and ε are functions of a as defined by (45), (50) and (51). Furthermore, we note that $a \equiv X/\tau$ in 1D and $a \equiv R/\tau$ in 2D.

It should be emphasized that (70) and (71) can be shown to agree with eqs. (4.3) and (5.6) of Berry (2005). Clarisse et al. (1995) focused from the very beginning on the response to delta-function disturbances, so their expressions can in priciple be retrieved by using $\Gamma_{1\delta} = 1/(4\pi)$ and $\Gamma_{2\delta} = 1/(2\pi)$. There is, however, generally a factor 2π difference between the results of Clarisse et al. and (70) and (71). Furthermore, for some reason they did not apply (53) for G_1 but promoted the approximation $G_1 \simeq \varepsilon/(1-a)$.

Figure 2 shows the variation of κ_0, u_0 and ε as a function of a according to (45), (50) and (51). The kinks at $a = 1$ for the continuations of κ_0 and u_0 are typical for functions jumping from the real axis to the imaginary axis at this location.

Figure 3 shows the variation of $G_1[u_0]$ as a function of a according to (53). The polynomial approximation (59) is accurate within $0.5 < a \leq 1$. The figure also includes the approximation $G_1 \simeq \varepsilon/(1-a)$ suggested by Clarisse et al. (1995), but this is seen to be very inaccurate and cannot be recommended.

Figure 4 shows the spatial variation of the 1D surface elevation as a function of $a = X/\tau$ at time $\tau = 100$ for the special case of an initial delta-function disturbance. We compare ζ_3 given by (12) and ζ_7 given by (70) and notice a remarkable agreement for $a < 0.95$. This clearly demonstrates that the uniform transformation is able to capture the full dispersion rather than just the KdV dispersion which was shown in Figure 1.

5. Convolution in one and two dimensions

For simple initial disturbances such as Gaussian distributions, it is straight forward to determine $\Gamma_1[\kappa]$ and $\Gamma_2[\kappa]$ analytically on the basis of (6) and (30). In this case the resulting surface elevation can be determined either by direct numerical integration of (8) and (29) or from the asymptotic approximations (70) and (71). However, in more general

cases, $\Gamma_1[\kappa]$ and $\Gamma_2[\kappa]$ cannot be determined analytically, and here we use the delta-function formulations combined with convolution integrals as described in the following.

5.1. Convolution in 1D

To solve the 1D problem of an initial condition given as $\zeta[X,0] = F[X]$, we utilize convolution integration based on the impulse-response function ζ_7 with the delta function located at the origin. This is defined by (70) combined with $\Gamma_{1\delta} = 1/(4\pi)$. Typically, we can assume that $F[X] \neq 0$ for $X_{\min} \leq X \leq X_{\max}$ and identical to zero outside this interval. In this case the convolution integral reads

$$\widetilde{\zeta}[X_0,\,\tau] = \int_{X_{\min}}^{X_{\max}} F[X]\zeta_7\left[X_0 - X,\,\tau\right] dX, \tag{72}$$

where X_0 is the observation coordinate, X is the integration coordinate covering the source region and ζ_7 is given by (70). In order to speed up the procedure, we first create interpolation functions for $\varepsilon[a]$ and $G_1[u_0]$ covering the interval $0 < a < 2.5$, and secondly we evaluate the integral numerically as

$$\widetilde{\zeta}[X_0,\,\tau] = \Delta X \sum_{X=X_{\min}}^{X_{\max}} F[X]\zeta_7\left[X_0 - X,\,\tau\right], \tag{73}$$

where the increments are chosen as

$$\Delta X = \frac{X_{\max} - X_{\min}}{n_x - 1}, \tag{74}$$

with n_x being the number of grid points.

5.2. Convolution in 2D

To solve the 2D problem of an initial condition given as $\zeta[X, Y, 0] = F[X, Y]$, we utilize convolution integration based on the radially symmetric impulse-response function ζ_{16} with the delta function located at the origin. This is defined by (71) combined with $\Gamma_{2\delta} = 1/(2\pi)$. The convolution formulation in rectangular coordinates reads

$$\widetilde{\zeta}[X_0,\, Y_0,\, \tau] = \int_{Y_{\min}}^{Y_{\max}} \int_{X_{\min}}^{X_{\max}} F[X,\, Y]\; \zeta_{16}\left[R[X,\, Y,\, X_0,\, Y_0],\, \tau\right] dX dY, \tag{75}$$

where $(X_0,\, Y_0)$ defines the observation point, $(X,\, Y)$ defines the integration coordinate covering the source region and R defines the distance between these points given by

$$R[X,\, Y,\, X_0,\, Y_0] = \sqrt{(X - X_0)^2 + (Y - Y_0)^2}. \tag{76}$$

In practise, we evaluate the double integral numerically by the double summation

$$\widetilde{\zeta}[X_0,\, Y_0,\, \tau] = \Delta X \Delta Y \sum_{X=X_{\min}}^{X_{\max}} \sum_{Y=Y_{\min}}^{Y_{\max}} F[X,\, Y]\; \zeta_{16}[R[X,\, Y,\, X_0,\, Y_0],\, \tau]. \tag{77}$$

The case is illustrated by Figure 5, where the observation point is located at O and the intial disturbance is located within the area with corner points A, B, C and D centered at the origin of the rectangular coordinate system $(X,\, Y)$. These corner points define the values of $X_{\min}$, $X_{\max}$, $Y_{\min}$ and $Y_{\max}$, while the discrete increments are given by

$$\Delta X = \frac{X_{\max} - X_{\min}}{n_x - 1}, \qquad \Delta Y = \frac{Y_{\max} - Y_{\min}}{n_y - 1}, \tag{78}$$

with e.g. n_x and n_y being the number of grid points.

One way to speed up the process is to introduce a local polar coordinate system (s, θ) centered at the observation point O i.e. at (X_0, Y_0). This leads to the coordinate transformation

$$X \equiv X_0 - s\cos\theta, \qquad Y \equiv Y_0 - s\sin\theta, \tag{79}$$

where s denotes the distance from (X_0, Y_0) to (X, Y). Now the convolution summation can take place in discrete s and θ increments e.g. within the sector of the annulus confined by the points E, F, G and H (see Figure 5). With ζ_{16} being radially symmetric i.e. independent of the angle θ this leads to the simplification

$$\widetilde{\zeta}[X_0,\, Y_0,\, \tau] = \Delta s \Delta\theta \sum_{s=R_{\min}}^{R_{\max}} \left(\sum_{\theta=\theta_{\min}}^{\theta_{\max}} F[X_0 - s\cos\theta,\, Y_0 - s\sin\theta] \right) s\zeta_{16}[s,\, \tau], \tag{80}$$

where

$$\triangle s = \frac{R_{\max} - R_{\min}}{n_R - 1}, \qquad \Delta\theta = \frac{\theta_{\max} - \theta_{\min}}{n_\theta - 1}. \tag{81}$$

The limits of $R_{\max}$, $R_{\min}$, $\theta_{\max}$, and $\theta_{\min}$ are readily determined from the location of the E, F, G and H points in Figure 5.

An alternative and even faster procedure is outlined in the following: First, the distance R between the observation point and each of the discrete integration points within the domain of the initial disturbance is determined. Now we have a map of associated {R, F} values representing distance and source values at all discrete integration points. Typically, a specific value of R will occur at several grid points and therefore be associated with several values of F. This is illustrated in Figure 6 (top panel), which shows the discrete values of F as a function of the associated values of R for the case of a Gaussian

disturbance. The next step is to cover the interval from $R_{\min}$ to $R_{\max}$ by increments of $\triangle s$ (as defined by (81)) and to sum up all F-values falling within these discrete Δs-bins. This leads to the accumulated source function

$$E[s] = \sum F[s], \tag{82}$$

which is illustrated in Figure 6 (bottom panel) for the case of a Gaussian disturbance. With this information at hand, we can simplify the double summation (77) to the single summation

$$\widetilde{\zeta}[X_0,\, Y_0,\, \tau] = \Delta X \Delta Y \sum_{s=R_{\min}}^{R_{\max}} E[s]\ \zeta_{16}[s,\, \tau]. \tag{83}$$

This procedure is extremely fast and provides the resulting time series in a few seconds.

6. Applications on a constant depth

6.1. The case of an initial 1D rectangular disturbance

We first consider a 1D sharp-edged rectangular disturbance described by $F[X] = F_0$ within $x_{\min} \le x \le x_{\max}$. This will generate a transient wave with a highly dispersive tail, and as reference, we apply a linear high-order Boussinesq model (see e.g. Madsen et al. 2002, Fuhrman & Bingham, 2004), which incorporates accurate dispersion properties up to dimensionless wave numbers of $\kappa = 25$. A similar test case was studied by Madsen & Schäffer (2010), their section 7.2. In dimensional variables, we use $h_0 = 4000$ m, $x_{\max} = -150$ km, $x_{\min} = -400$ km and consider the observation point $x_0 = 12,000$ km. This corresponds to the non-dimensional parameters $X_{\max} = -37.5$, $X_{\min} = -100$ and $X_0 = 3000$. It is emphasized that Madsen & Schäffer used an initial amplitude of 3 m, but this was combined with a reflecting wall at the input boundary so in the present

formulation this corresponds to $F_0 = 6/4000 = 0.0015$. The numerical Boussinesq solution is computed using a fixed grid of $dx = 400$ m, a time step of $dt = 2$ s, and a total of $40,001$ grid points and $40,001$ time steps. The convolution solution is obtained by using (73)-(74) with $n_x = 200$.

Figures 7a-b show a comparison of the linear Boussinesq solution (dashed line) and the convolution solutions (full gray lines). The top panel shows the performance of the non-uniform weakly dispersive formulation $\widetilde{\zeta}_4$ (given by (18)). This is fairly accurate for the first 60 min of the time series, but beyond this point discrepancies in phase and amplitude show up. The bottom panel shows the performance of the fully-dispersive uniform formulation $\widetilde{\zeta}_7$ (given by (70)). This is obviously more accurate than the non-uniform formulation. The differences between the two convolution solutions increases significantly when we continue the time series in Figures 8a-b, now covering from 1150 min to 1300 min. According to the top panel, the non-uniform formulation is now completely off in amplitude and phase, while the uniform formulation, shown in the bottom panel, is in very good agreement with the Boussinesq simulation. This confirms the accuracy of the uniform asymptotic approximation versus the conventional KdV-approximation.

6.2. The case of an initial 2D square disturbance

We continue with a square sharp-edged disturbance in 2D, which again is expected to generate a transient wave with a highly dispersive tail. The initial disturbance is shown in Figure 5, where the points A, B, C, D are located at $(b_1,\, b_1)$, $(b_1,\, -b_1)$, $(-b_1,\, -b_1)$, $(-b_1,\, b_1)$, with $b_1 = 32$ km and where the initial amplitude within this area is $a_1 = 16$ m. The volume of this initial disturbance is therefore $4a_1b_1^2$. The water depth is constant and equal to $h = 4.0$ km. The location of the observation points are generally specified by

$$x_0 = r_0 \cos\varphi_0, \quad y_0 = r_0 \sin\varphi_0. \tag{84}$$

Again we use the linear high-order Boussinesq model as reference, but this time we also include computations based on the non-dispersive linear shallow water model (Ren et al., 2013) in order to illustrate the influence of dispersion. Both models are set up to cover the first quadrant of the problem using 2000 by 2000 grid points with grid size $dx = dy = 1.0$ km and 3000 time steps with step size $dt = 5.0$ s. A perspective snapshot of the computed surface elevation is shown in Figure 9.

The convolution method covers the initial disturbance area with $n_x = n_y = 100$ grid points in rectangular coordinates and $n_R = n_\theta = 100$ grid points in polar coordinates. Double summation of (77) in rectangular coordinates takes approximately 400 s, while double summation of (80) in polar coordinates takes about 30 s. Finally, the single summation (83) takes about 4 s. Results obtained by the three different convolution methods are virtually identical and consequently only the single summation results are shown.

Figures 10a-d show the computed temporal variation of the surface elevation at four locations defined by $r_0 = 600$ km and $\varphi_0 = 0$, $\pi/16$, $\pi/8$ and $\pi/4$ respectively. We notice that the dispersive tail of the wave train is much stronger for small angles in contrast to the case of $\varphi_0 = \pi/4$ where it is almost absent. The convolution solution based on (83) is shown as gray lines, the linear Boussinesq results as black lines and the linear shallow water results as dashed lines. Generally, there is very little difference between the convolution solution and the Boussinesq results. We notice that the non-dispersive shallow water model can only represent the leading wave, and this is typically overestimated if

the tail is present in the reference solution (as e.g. for $\varphi_0 = 0$), while it is more accurate if the tail is small (as e.g. for $\varphi_0 = \pi/4$).

Figures 11a-c show the computed temporal variation of the surface elevation at another three locations defined by $\varphi_0 = 0$, and $r_0 = 400$ km, 800 km and 1200 km, respectively. Small discrepancies between the convolution solution and the linear Boussinesq results can be seen at the first location, while the solutions are almost identical further away from the origin. Again we can conclude that the uniform asymptotic approximation is very accurate. The linear shallow water model is significantly off at all three locations.

6.3. The case of an initial 2D Gaussian disturbance

Next, we consider the case of a blunt Gaussian disturbance defined by

$$F[r] = a_2 \exp\left[-\frac{r^2}{b_2^2}\right] \qquad \text{or} \qquad F[x,y] = a_2 \exp\left[-\left(\frac{x^2+y^2}{b_2^2}\right)\right]. \tag{85}$$

The limiting points A, B, C, D (see Figure 5) are now located at $(3b_2,\, 3b_2)$, $(3b_2,\, -3b_2)$, $(-3b_2,\, -3b_2)$, $(-3b_2,\, 3b_2)$ and to obtain the same volume as in the previous square case we choose

$$b_2 = \sqrt{\frac{2}{3}}\, b_1, \qquad a_2 = \frac{6}{\pi} a_1, \tag{86}$$

with $b_1 = 32$ km, $a_1 = 16$ m, $h = 4$ km. Convolution covers the initial disturbance area with $n_x = n_y = 100$ grid points in rectangular coordinates and $n_R = n_\theta = 100$ grid points in polar coordinates.

With the initial condition being radially symmetric, we now have several options for calculating the impact. First of all, (30) integrates to

$$\Gamma_2[\kappa] = \frac{1}{2}\frac{a_1 b_1^2}{h^3}\exp\left[-\frac{b_1^2\kappa^2}{4h^2}\right], \tag{87}$$

which makes it possible to use direct numerical integration of (29). This procedure was recently pursued by Tobias & Stiassnie (2011). Figure 12a shows this solution (full black line) at the observation point $r_0 = 600$ km (i.e. $R_0 = 150$) and $\varphi_0 = \pi/4$. The linear high-order Boussinesq simulation (setup as in the previous square case) is shown as dashed black line. The agreement is outstanding. We have checked the Boussinesq result at other angles but for approximately the same distance, and as expected these results are almost identical due to the axis-symmetry of the source.

As a second possibility, we can use convolution by double summation in rectangular coordinates i.e. (77), convolution by double summation in polar coordinates i.e. (80) or convolution by single summation i.e. (83). Generally, these convolution methods are utilizing $\Gamma_{2\delta} = 1/(2\pi)$ combined with the uniform approximation ζ_{16} (defined by (71)). As concluded in the previous test case, results obtained by the three different convolution methods are virtually identical and consequently only the single summation results are shown. Figure 12b shows that the uniform convolution solution (dashed line) is in excellent agreement with the direct numerical integration (full line).

Notice that due to the bluntness of the Gaussian disturbance only a leading wave is seen and the dispersive tail is practically missing. Obviously, this means that there is no need for the full dispersion incorporated in the uniform method. To illustrate this point, we re-calculate the single summation convolution with the non-uniform weakly dispersive version of (71), which reads

$$\zeta_{17}[a,\tau] = -\frac{1}{\tau\sqrt{a}} Ai\left[-(1-a)2^{-1/3}\tau^{2/3}\right] Ai'[-(1-a)2^{-1/3}\tau^{2/3}].$$

Figure 12c shows that this result is also in excellent agreement with (29).

As a final possibility, we can use ζ_{16} (defined by (71)) directly as an analytical expression with Γ_2, defined by (87) and evaluated at the stationary points $\kappa = \kappa_0$. This is by far the fastest method for Gaussian disturbances. However, Figure 12d shows that it leads to a significant overestimate and phase-shift of the leading wave compared to the direct numerical integration. This may come as a surprise considering that Berry (2005) found excellent agreement with numerical integration in all his test cases. The reason is, however, that Berry only considered very narrow Gaussian shapes. With the present, much wider, Gaussian shape, the accuracy of this procedure is poor, although it gradually improves with increasing distances from the event. For the present source, we have found that this method overestimates the peak of the leading wave by 60% for $r_0 = 600$ km, 32% for $r_0 = 1200$ km, 19% for $r_0 = 2400$ km, 14% for $r_0 = 3600$ km, and 10% for $r_0 = 6000$ km.

Even though the relatively wide Gaussian disturbance generates a transient wave with almost no dispersive tail in the near field (as seen in Figures 12a-d), the dispersive tail will gradually grow during the propagation over large distances. To illustrate this point, Figures 13a-c show a comparison of the different solutions at the observation point $r_0 = 6000$ km (i.e. $R_0 = 1500$) and $\varphi_0 = \pi/4$. Figure 13a shows again an excellent agreement between the direct numerical integration and the single summation convolution combined with the uniform expression ζ_{16}. In contrast, Figure 13b shows that the single summation convolution combined with the non-uniform expression ζ_{17} starts to become inaccurate. Finally, Figure 13c shows that the direct use of (71) with (87) starts to become more

accurate, but even with such a large distance to the event discrepancies can still be seen. We therefore do not recommend this method. Speedwise the direct numerical integration takes about $200-400$ s, while the single summation convolution (83) takes about $3-5$ s.

7. Convolution formulation for geophysical problems

7.1. Extension of the convolution method to an uneven bottom

Geophysical large-scale problems call for a number of modifications of the methods presented so far, partly because the waves propagate on the surface of a sphere, and partly because the water depth is not constant.

The first issue is related to distances on a curved surface and it is easily incorporated in the model: Locations are typically defined in spherical coordinates e.g. longitude/latitude degrees (θ, φ) and the radius of the Earth ($R_E = 6371000$ m). These are related to the Cartesian coordinate system by

$$(x,\, y,\, z) = R_E\,(\cos\varphi\cos\theta,\ \cos\varphi\sin\theta,\ \sin\varphi)\,. \tag{88}$$

The shortest curved distance between two locations (A and O) on the sphere is along the segment of the great circle joining them and it is determined by

$$r_{AO} = \phi_{AO} R_E, \tag{89}$$

where ϕ_{AO} defines the angle ACO (in radians) with C being the center of the sphere. This angle is determined by

$$\cos[\phi_{AO}] = \cos[\varphi_A]\cos[\varphi_O]\cos[\theta_A-\theta_O] + \sin[\varphi_A]\sin[\varphi_O]. \tag{90}$$

The second issue is related to geometrical spreading and it is also easily incorporated in the model: For a disturbance radiating from a point source on a flat surface, the conservation of energy flux along the perimeter of the expanding circle will make the wave amplitude decay with the distance to the power $-1/2$. This feature is clearly incorporated in (71). However, when the disturbance moves on a sphere, the effective perimeter of the small circle will be $2\pi R_E \sin[\phi_{AO}]$ rather than $2\pi r_{AO}$ and therefore the response function (71) needs to be multiplied by the spreading factor

$$\alpha_{AO} = \sqrt{\frac{\phi_{AO}}{\sin[\phi_{AO}]}}. \tag{91}$$

The third, and most important, issue is related to the fact that the water depth $h[\theta, \varphi]$ is generally not constant and as a result shoaling, refraction and diffraction may be important. Diffraction can only be incorporated for idealized canonical bathymetries and even in this case it is not a trivial task (see e.g. Berry, 2007). Refraction is also very difficult to incorporate as it would require that we track each radiating beam from source to observation point. We have therefore chosen to ignore refraction/diffraction and focus on the incorporation of linear shoaling and its influence on the travel time of the leading wave.

As a starting point, we assume that each discrete source point (A) will result in a wave disturbance travelling along a straight transect of the bathymetry from A to the relevant observation point O. This is obviously a crude approximation, which may be violated in case of refraction (and diffraction). We resolve the transect with typically $N = 300 - 500$ discrete points and integrate the linear shallow water celerity to obtain the following estimate of the arrival time (travel time) of the first disturbance

$$t_{AO} = \frac{r_{AO}}{N}\sum_{j=0}^{N}\frac{1}{\sqrt{gh[\theta_j,\,\varphi_j]}}, \tag{92}$$

where

$$\theta_j \equiv \theta_O + \frac{j}{N}(\theta_A - \theta_O), \quad \varphi_j \equiv \varphi_O + \frac{j}{N}(\varphi_A - \varphi_O). \tag{93}$$

The corresponding mean water depth (d_{AO}) associated with each transect is now determined from

$$\sqrt{gd_{AO}} = \frac{r_{AO}}{t_{AO}}. \tag{94}$$

Finally, linear shoaling along each transect is approximated by Green's law i.e.

$$\beta_{AO} = \left(\frac{h[\theta_O, \varphi_O]}{h[\theta_A, \varphi_A]}\right)^{-1/4}. \tag{95}$$

We emphasize that this approach is based on non-dispersive linear shallow water theory. This is to some extent justified by the fact that natural tsunami sources often appear with relatively mild spatial gradients leading to relatively weak dispersion in the leading waves. With this in mind, there is no reason to expect that the resulting uneven bottom version of the uniform asymptotic approximation will perform any better than a version based on the classical non-uniform asymptotic approximation. At this point, our goal is simply to investigate the ability of these models to predict the leading waves of the geophysical tsunami.

The fourth issue is the grid resolution of the source region: This is typically given in longitude/latitude degrees as

$$\Delta\theta = \left(\frac{\theta_{\max} - \theta_{\min}}{n_\theta - 1}\right), \qquad \Delta\varphi = \left(\frac{\varphi_{\max} - \varphi_{\min}}{n_\varphi - 1}\right), \tag{96}$$

and we need to convert it, first to meters and secondly by normalizing with the mean water depth. This leads to

$$\Delta X = \frac{\gamma\Delta\theta}{d_{AO}}\cos[\varphi_A], \qquad \Delta Y = \frac{\gamma\Delta\varphi}{d_{AO}}, \qquad \gamma = \frac{2\pi R_E}{360}. \tag{97}$$

Note that (89)-(97) should be applied in each discrete source point A with coordinates (θ_A, φ_A) to provide maps of e.g. distance, travel time, mean depth, spreading index, shoaling index and local grid resolution for any specific choice of the observation point O. As a consequence, we modify the original source map F_A as follows

$$F_{AO} = \frac{\gamma^2\Delta\theta\Delta\varphi\cos[\varphi_A]}{d_{AO}^2}\alpha_{AO}\beta_{AO}F_A. \tag{98}$$

The impulse response function ζ_{16} was defined by (71) as a function of R and τ, but fundamentally it is a function of a and τ. On a constant depth, a is defined as

$$a = \frac{R}{\tau}, \quad \text{where} \quad R = \frac{r}{h_0} \quad \text{and} \quad \tau = t\sqrt{\frac{g}{h_0}},$$

but on an uneven bottom, we replace h_0 by d_{AO} and r by r_{AO}, which leads to

$$a[\theta_A, \varphi_A, t] = \frac{t_{AO}[\theta_A, \varphi_A]}{t}, \quad \text{and} \quad \tau[\theta_A, \varphi_A, t] = t\sqrt{\frac{g}{d_{AO}[\theta_A, \varphi_A]}}. \tag{99}$$

On this basis, we modify the double summation convolution (77) to

$$\eta_O[t] = \sum_{\theta_A=\theta_{\min}}^{\theta_{\max}} \sum_{\varphi_A=\varphi_{\min}}^{\varphi_{\max}} F_{AO}[\theta_A, \varphi_A]\ \zeta_{16}\left[a,\, \tau\right], \tag{100}$$

where a and τ are determined by (99) and where $\eta_O[t]$ is the resulting surface elevation (in meters) at the observation point O.

As long as the conversion from t to τ depends on the local mean depth d_{AO} in the source area, we cannot simplify the double summation convolution to a single summation convolution. However, often the variation of d_{AO} is quite limited, and if this is the case we can use the approximation

$$\tau[t] \simeq t\sqrt{\frac{g}{d_{AO}[\theta_{peak}, \varphi_{peak}]}}, \tag{101}$$

where $(\theta_{peak}, \varphi_{peak})$ defines the location of the peak source. This leads to the following simplifications: First, we consider the map of associated $\{t_{AO},\, F_{AO}\}$ values representing arrival time and source values at all discrete source points. Second, we cover the interval from $t_{\min}$ to $t_{\max}$ by increments of $\triangle s$ and sum up all F_{AO}-values falling within these discrete Δs-bins. This leads to the accumulated source function

$$E[s] = \sum F_{AO}[s], \quad \text{where} \;\; t_{\min} \le s \le t_{\max}. \tag{102}$$

The resulting single summation convolution reads

$$\eta_O[t] = \sum_{s=t_{\min}}^{t_{\max}} E[s]\; \zeta_{16}\left[\frac{s}{t}, \tau\right], \tag{103}$$

where τ is given by (101). Again this is an extremely fast procedure which can provide the resulting time series in a matter of seconds.

7.2. Applications on the 2011 Japan tsunami

In order to test the validity of our convolution approach extended to uneven bottom, we study the 2011 Japan tsunami. For this purpose we have chosen to apply the UCSB source by Shao et al. (2011) covering the longitude/latitude area of $140 \leq \theta_A \leq 145$ degrees and $35 \leq \varphi_A \leq 41$ degrees with $40,000$ gridpoints. Ren et al. (2013) used the same source for their simulations with a model based on the nonlinear shallow water (NSW) equations, and their results make a good benchmark in combination with the variety of deep water DART measurements in the Pacific.

The UCSB source is instantaneously triggered at 2.46 PM JST (05.46 UTC) on March 11th, 2011. The maximum elevation specified by this source is 15.88 m and occurs at $(\theta_{peak}, \varphi_{peak}) = (143.593,\ 38.5578)$. Figure 14 shows a perspective plot of the UCSB source given in meters as a function of the longitude/latitude coordinates, while Figure 15 shows the local bathymetry in the source region with the overlay of the source contours. As observation points we consider the following deep water DART buoys: 21418, 21401, 21419, 21413, 21415, 52402, 51407, 46404, 46411 and 51406, which are located as indicated on Figure 16. For each of these observation points the procedure defined by (89)-(101) is executed. As an example Figures 17a-c show the modified and accumulated source E determined by (102) and (98) as a function of the travel time to the observation points DART 21401, 21415 and 52402. Generally, we have used double summation as well as single summation convolution and there is hardly any difference for these cases, so only the single summation results are shown in the following.

Figures 18a-f focus on the near-field DART bouys 21418, 21401, 21419, 21413, 21415 and 52402, which are reached by the tsunami within 0.5 hours to 3.5 hours of travel

time. Observations (black) are compared with the convolution results (red) and the NSW simulations (green) by Ren et al. (2013). In stations 21401 and 21413 the two models agree quite well and they are both in pretty good agreement with the measurements. In stations 21415 and 52402 the amplitude of the leading wave tends to be overestimated by the convolution model, while it is smaller in the NSW simulations and thus in better agreement with the measurements. This trend is in contrast to our earlier comparison of the two models involving propagation on a constant depth (see Figures 10a-d and 11a-c). We assume that the reason is refraction effects, which are omitted in the convolution method. The arrival times of the two models are almost the same and typically slightly earlier than the observations. Overall, we may conclude that both models are applicable in the near field.

Figures 19a-d focus on the far-field DART bouys 51407, 46404, 46411 and 51406, which are reached by the tsunami within 7.5 hours to 14 hours of travel time. At stations 51407 and 46411 the convolution calculations (red) and the NSW simulations (green) deviate significantly in amplitude as well as in arrival time, and both are quite different from the measurements (black). The fact that the two calculations deviate so much again implies again that refraction (diffraction) effects cannot be ignored in the far field. The convolution approach assumes that disturbances travel along transects connecting the source points and the observation points, and while this is correct on a flat bottom it is not neccessarily a good approximation on a uneven bottom, where waves may take different paths. Furthermore, due to refraction a wave signal radiating in all directions from a point source may arrive at the observation point from several directions and with different time lags, and this is again not taken into account by the convolution model.

We conclude that the convolution model is not applicable in the far field if significant refraction and diffraction effects are present.

On the other hand, it should also be emphasized that the far-field NSW model results are far from impressive. Løvholt et al. (2012) used a different source distribution and achieved much better agreement e.g. at location 51407. They modelled the Tohoku tsunami with a linear weakly dispersive Boussinesq model and a linear non-dispersive shallow water model and both sets of results were generally found to be superior to the results by Ren et al. (2013). This clearly implies that the UCSB source used in the present work is not sufficiently accurate.

8. Summary and conclusion

In this work, we have presented a semi-analytical method for the linear and fully-dispersive propagation of waves over constant depth due to an initial surface displacement. In the first part (sections 2-4), we have re-derived impulse response functions for the 1D and 2D linear Cauchy-Poisson problem on a constant depth. The derivation utilizes integral formulations combined with the method of stationary phase, the method of uniform approximations and various Airy integral formulations. The resulting formulation is very efficient and highly accurate, incorporating full dispersion.

In the second part (sections 5-6), we have presented three different convolution techniques in order to deal with initial surface elevations of arbitrary shape on a constant depth. The most efficient of these techniques effectively reduces the 2D problem to a 1D problem, and determines the solution within a few seconds on a standard desktop computer. The procedure is first tested on a 1D rectangular disturbance and a 2D square disturbance. Both events are sharp-edged and generate a transient wave with a highly

dispersive tail, and they are therefore well suited to test the dispersion properties of the uniform asymptotic approximations. Results are compared to numerical simulations with a linearized high-order Boussinesq model, and the agreement is found to be excellent. In comparison, numerical simulations with the linear shallow water model fail to capture the dispersive tail as well as the temporal development of the leading waves.

Secondly, we consider the case of a wide Gaussian disturbance in 2D, which allows for a direct numerical integration, a direct analytical formulation, and three different convolution formulations. In the near field, this case will result in transient waves dominated by a single leading wave and with almost no dispersive tail. This implies that the classical non-uniform and weakly dispersive formulations of Kajiura (1963) and Whitham (1974) will do acceptably for this case, which is confirmed by our calculations. In the far field, however, the dispersive tail will grow and the non-uniform formulation will start to become inaccurate. Hence, we conclude that even for rather blunt disturbances dispersion will eventually play a role. We conclude that the proposed single summation convolution method combined with the uniform asymptotic impulse response function is superior in terms of flexibility, speed and accuracy for linear fully-dispersive transient problems on a constant depth.

Finally, we have made a first effort to extend the convolution method to geophysical problems (section 7). Various effects associated with the motion on a sphere and the motion over an uneven bottom have been incorporated. Of these, the uneven bottom is by far the most problematic to incorporate. In our extension, we have neglected refraction/diffraction while approximating shoaling via linear shallow water theory. This leads to fairly simple estimates of travel time and travel paths connecting the source and obser-

vation points by straight transects. The modified convolution procedure has been tested on data from the 2011 Japan tsunami from ten DART buoys in the Pacific and it has been compared to NSW simulations based on the same tsunami source. It turns out that results agree fairly well with observations within the near field i.e. for locations within 0.5 hours to 3.5 hours of travel time. It is, however, also clear that far-field results (within 7.5 hours to 14 hours) are quite poor: The travel time is clearly underestimated and the time signals deviate from observations as well as from the NSW simulations. We conclude that far-field locations are quite sensitive to refraction (and diffraction) effects, which make the disturbances travel along a diversity of paths before reaching the observation point. Such effects are important to recognize, though they are unfortunately beyond the reach of the present convolution procedure.

Acknowledgments. The following contributions to this work are highly appreciated: Sir M.V. Berry and Dr J.-M. Clarisse clarified various aspects of their original works from 2005 and 1995 via several email communications. Prof. Hua Liu and Zhiyuan Ren kindly provided data from their study of the Japan 2011 tsunami. Dr. D.R. Fuhrman acknowledges support from the European Union project ASTARTE, Grant no. 603839 (FP7-ENV-2013.6.4-3). The DART measurements can be obtained from the NOAA site www.ndbc.noaa.gov/dart.shtml. All remaining data used in this paper can be obtained by email request to the first author at prm@mek.dtu.dk.

References

Berry, M.V. 2005 Tsunami asymptotics. *New Journal of Physics,* **7**, 129.

Berry, M.V. 2007 Focused tsunami waves. *Proc. Roy. Soc. Lond. A*, **463**, 3055-3071.

Bleistein, N. 1967 Uniform asymptotic expansions of integrals with many nearby stationary points and algebraic singularities. *J. Mathematics and Mechanics,* **17 (6)**, 533-559.

Bleistein, N. 1966 Uniform asymptotic expansion of integrals with stationary point and nearby algebraic singularity. *Comm. Pure Appl. Math.,* **19**, 253.

Chester, C., Friedman, B. and Ursell, F. 1957 An extension of the method of steepest descents. *Math. Proc. Camb. Phil. Soc.,* **53**, 599-611.

Child, M.S. 1975 A uniform approximation for one-dimensional matrix elements, *Mol. Phys.* **29**, 1421-1429.

Clarisse, J.-M., Newman, J.N. and Ursell, F. 1995 Integrals with a large parameter: water waves on finite depth due to an impulse. *Proc. Roy. Soc. Lond. A*, **450**, 67-87.

Fuhrman, D.R. and Bingham, H.B. 2004 Numerical solutions of fully nonlinear and highly dispersive Boussinesq equations in two horizontal dimensions. *Int. J. Numerical Methods in Fluids*, **44**, 231-255.

Glimsdal, S., Pedersen, G.K., Langtangen, H.P., Shuvalov, V. and Dypvik, H. 2007 Tsunami generation and propagation from the Mjølnir asteroid impact. *Meteoritics and planetary science*, **42 (9)**, 1473-1493.

Glimsdal, S., Pedersen, G.K., Harbitz, C.B. and Løvholt, F. 2013 Dispersion of tsunamis: does it really matter? *Nat. Hazard Earth Syst. Sci.*, **13**, 1507-1526.

Grilli, S.T., Harris, J.C., Bakhsh, T.S.T., Masterlark, T.L., Kyriakopoulos, C., Kirby, J.T. and Shi, F. 2013 Numerical simulation of the 2011 Tohoku tsunami based on a new transient FEM co-seismic source: Comparison to far- and near-field observations. *Pure Appl. Geophys.*, **170**, 1333-1359.

Kajiura, K. 1963 The leading wave of a tsunami. *Bull. Earthquake Res. Inst.*, University of Tokyo, **41**, 525-571.

Kuznetsov, N. 2006 Asymptotic analysis of rapid forward accelerations of a free-surface pressure. *J. of Engineering Mathematics*, **55**, 167-181.

Lamb, H. 1932 *Hydrodynamics*, 6th ed. Cambridge University Press.

LeBlond, P.H. and Mysak, L.A. 1978 *Waves in the ocean*, Elsevier, New York.

Løvholt, F., Kaiser, S., Glimsdal, S., Scheele, L., Harbitz, C.B. and Pedersen, G. 2012, Modelling propagation and inundation of the 11 March 2011 Tohoku tsunami, *Nat. Hazard Earth Syst. Sci.*, **12**, 1017-1028.

Madsen, P.A., Bingham, H.B. and Liu, H. 2002 A new Boussinesq method for fully non-linear waves from shallow to deep water. *J. Fluid Mech.*, **462**, 1-30.

Madsen, P.A., Fuhrman, D.R. and Schäffer, H.A. 2008 On the solitary wave paradigm for tsunamis. *J. Geophysical Research*, **113**, C12012, 1-22.

Madsen, P.A. and Schäffer, H.A. 2010 Analytical solutions for tsunami runup on a plane beach: single waves, N-waves and transient waves. *J. Fluid Mech.*, **645**, 27-57.

Newman, J.N. 1991 Asymptotic approximations of the Cauchy-Poisson problem. In *Mathematical approaches in hydrodynamics*, 225-237, Philadelphia, PA: SIAM.

Ren, Z., Wang, B., Fan, T. and Liu, H. 2013 Numerical analysis of impacts of 2011 Japan Tohoku tsunami on China Coast, *J. Hydrodynamics*, **25 (4)**, 580-590.

Shao, G., Li X., Ji C. Maeda, T. 2011 Focal mechanism and slip history of 2011 Mw 9.1 off the Pacific coast of Tohoku earthquake, constarined with teleseismic body and surface waves. *Earth Planets Space*, **63**, 559-564.

Sekerzh-Zenkovich, S.Y. 2009 Simple asymptotic solution of the Cauchy-Poisson problem for head waves. *Russian Journal of Mathematical Physics*, **16 (2)**, 315-322.

Stokes, G.G. 1850 On the numerical calculation of a class of definite integrals and infinite series, *Trans. Camb. Phil. Soc.,* **9**, 166-187 (see also Mathematical and Physical papers, vol. 2, p. 341).

Tang, L., Titov, V.V., Bernard, E.N., Wei, Y., Chamberlin, C.D., Newman, J.C., Mofjeld, H.O., Arcas, D., Eble, M.C., Moore, C., Uslu, B., Pells, C., Spillane, M., Wright, L. and Gica, E. 2012 Direct energy estimation of the 2011 Japan tsunami using deep-ocean pressure measurements. *J. Geophysical Research*, **117**, C08008, 1-28.

Thomson, W. 1887 On the waves produced by a single impulse in water of any depth, or in a dispersive medium. Proc. Roy. Soc. xlii. 80 (see also Mathematical and Physical papers, vol 4, p. 303).

Tobias, J. and Stiassnie, M. 2011 An idealized model for tsunami study. *J. Geophysical Research*, **116**, C06026, 1-9.

Ursell, F. 1965 Integrals with a large parameter. The continuation of uniformly asymptotic expansions. *Math. Proc. Camb. Phil. Soc.*, **61**, 113-128.

Ursell, F. 1980 Integrals with a large parameter: a double complex integral with four nearly coincident saddle-points. *Math. Proc. Camb. Phil. Soc.*, **87**, 249-273.

Ursell, F. 2007 Water wave problems, their mathematical solution and physical interpretation. J. Eng. Math., 58, 7-17.

Vallée, O. and Soares, M. 2004 *Airy functions and applications to physics.* World Scientific, Singapore.

Wehausen, J.V. and Laitone, E.V. 1960 Surface waves. In *Encyclopedia of physics*, **9**, 446-778.

Whitham, G.B. 1974 *Linear and nonlinear waves.* New York: Wiley-Interscience.

Wong, R. 1989 *Asymptotic approximations of integrals.* Academic Press, New York.

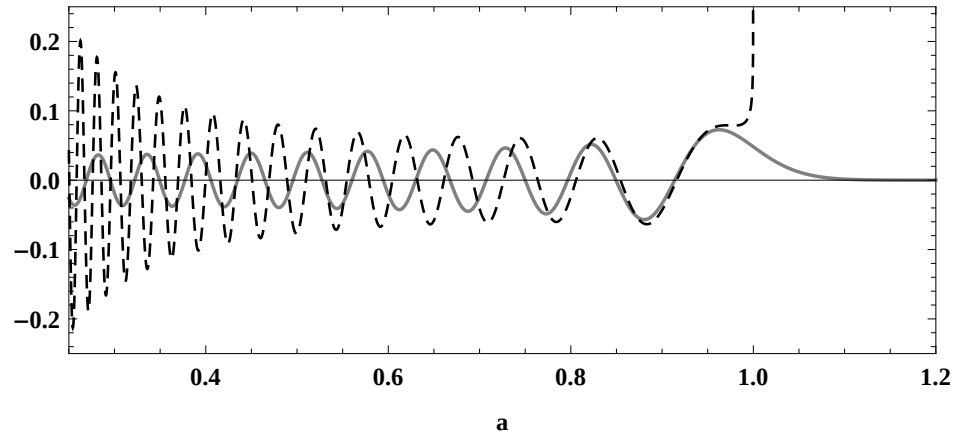

Figure 1. The 1D impulse response functions corresponding to a δ-function disturbance. Results obtained as a function of $a = X/\tau$ for $\tau = 100$. Full line: The weakly dispersive asymptotic approximation ζ_4 based on eq. (18); Dashed line: The classical asymptotic approximation ζ_3 based on eq. (12).

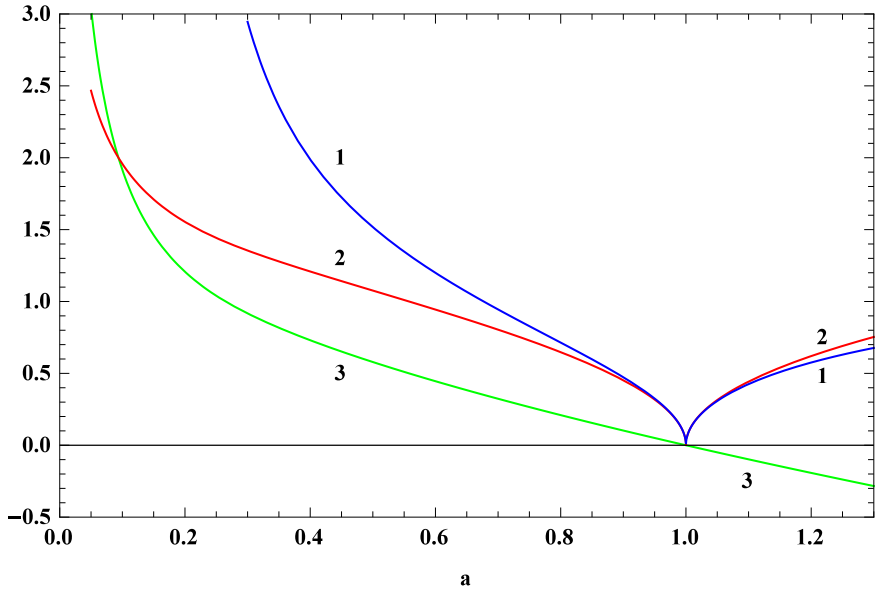

Figure 2. The variation of κ_0 (1), u_0 (2) and ε (3) as a function of $a = X/\tau$.

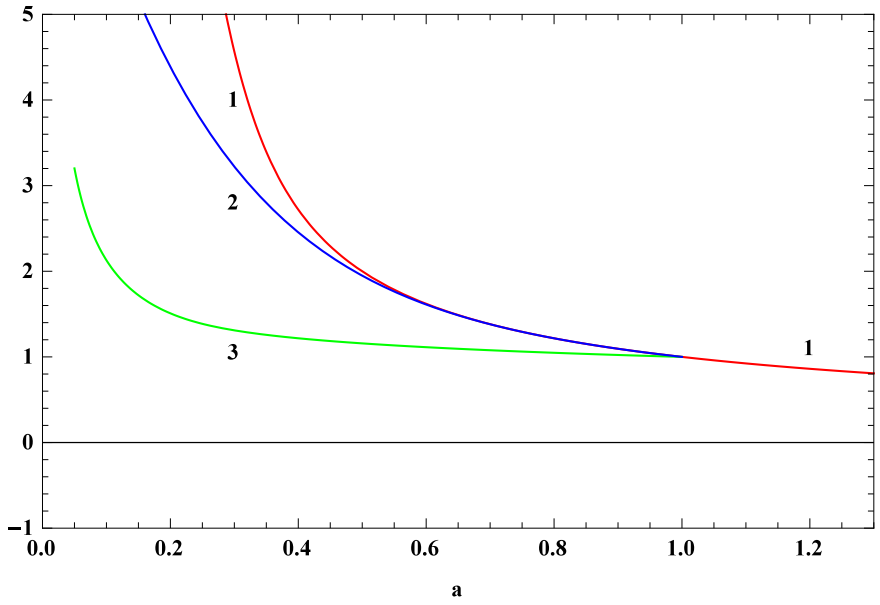

Figure 3. The variation of $G_1[u_0]$ as a function of $a = X/\tau$. (1) Full solution according to eq. (53) including extension into the complex domain according to eq. (69); (2) Taylor approximation according to eq. (59); (3) The approximation proposed by Clarisse et al. (1995) i.e. $\varepsilon/(1-a)$.

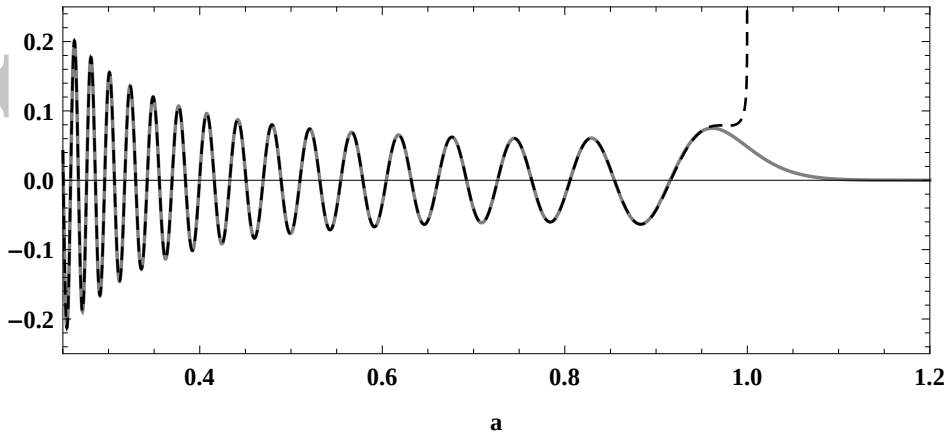

Figure 4. The 1D impulse response functions corresponding to a δ-function disturbance. Results obtained as a function of $a = X/\tau$ for $\tau = 100$. Full line: The uniform (fully dispersive) asymptotic approximation ζ_7 based on eq. (70); Dashed line: The classical asymptotic approximation ζ_3 based on eq. (12).

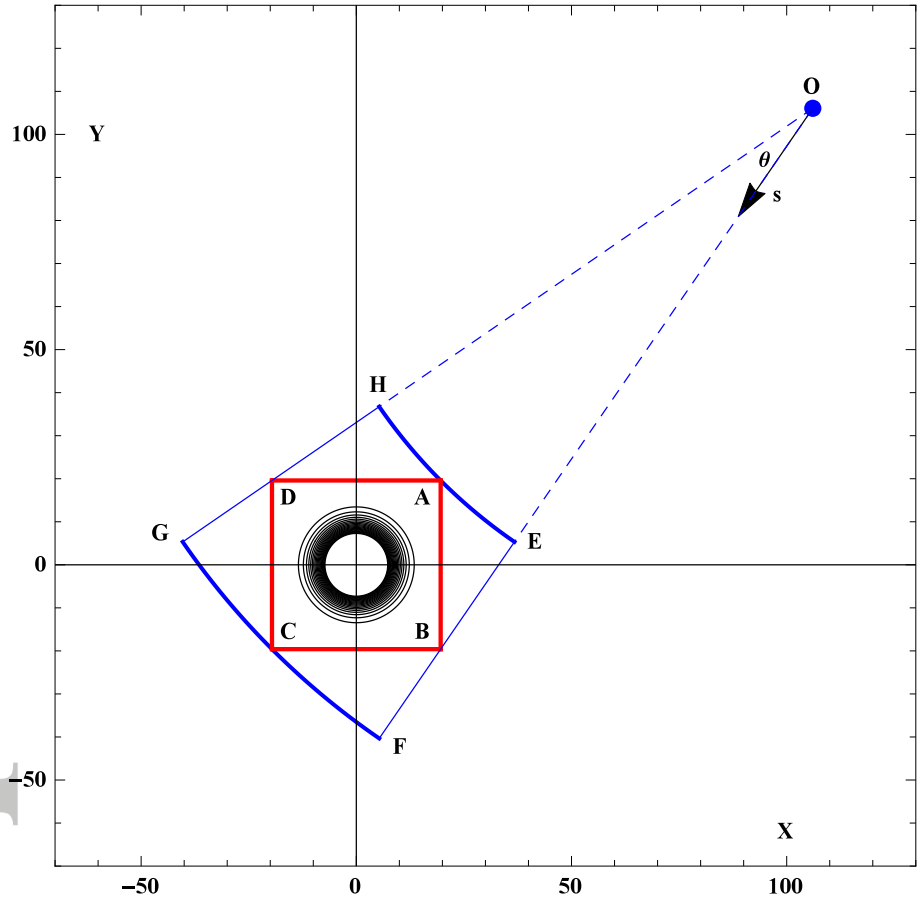

Figure 5. Sketch illustrating the convolution procedure in 2D. As an example, an initial Gaussian disturbance is contained in the square with corner points A, B, C and D. The integration points are expressed in local polar coordinates with the observation point O as origin. Actual convolution integration takes place within the sector of the annulus (confined by the points E, F, G and H).

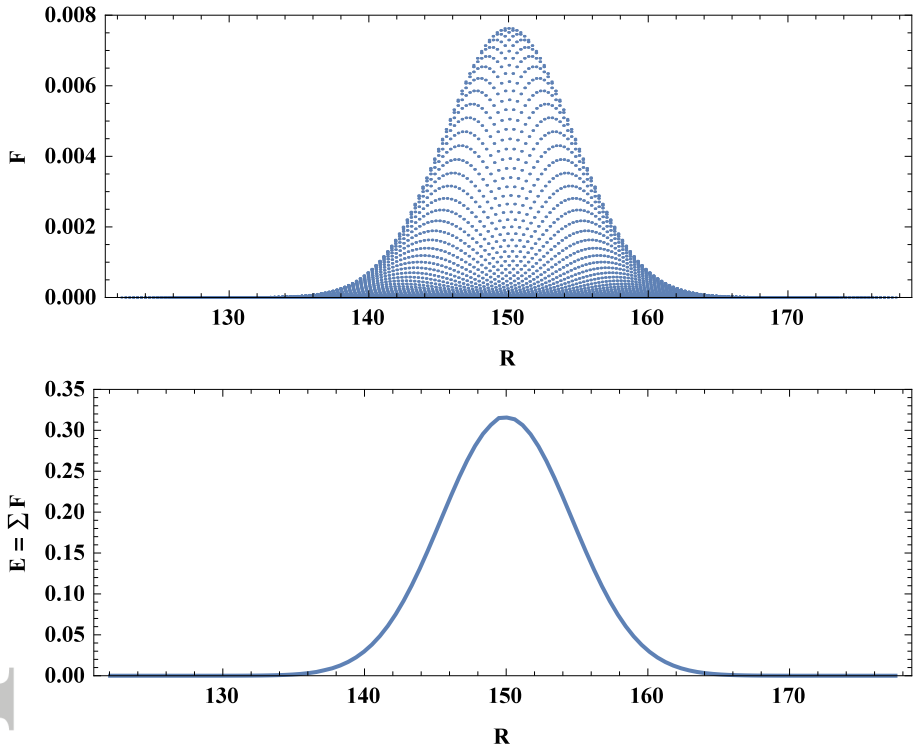

Figure 6. The discrete values of an initial Gaussian disturbance F shown as a function of the associated distance R from the selected observation point to each of the integration points. Top panel: F as a function of R; Bottom panel: Sum of F within discrete R bins based on eq. (82).

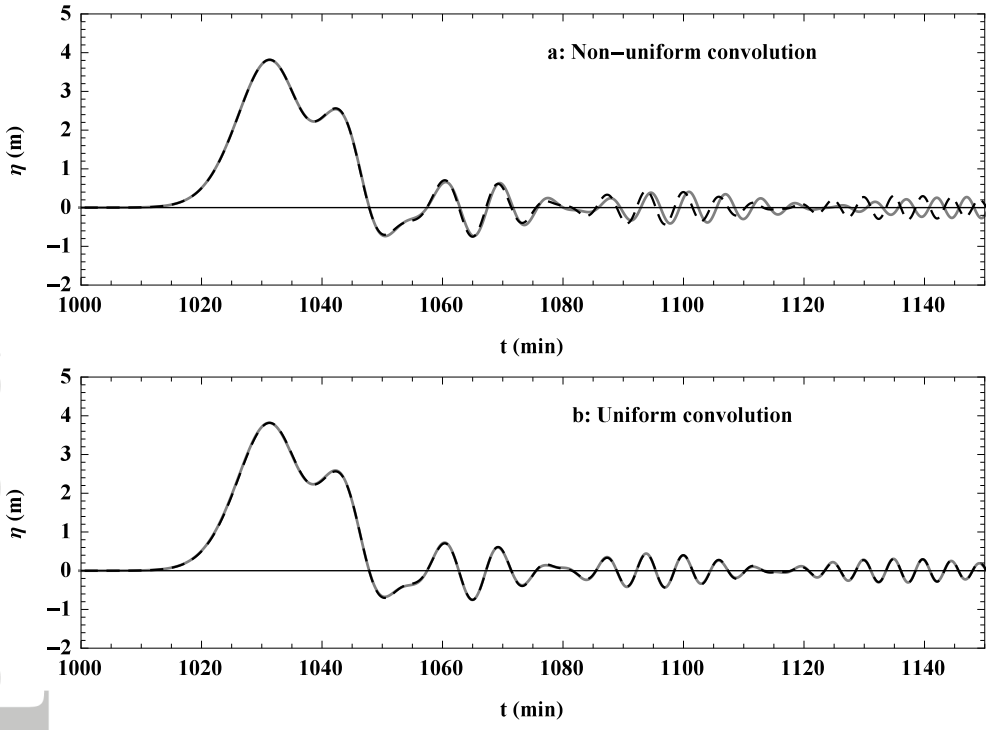

Figure 7. First part of the time series of the surface elevation due to a monopole source. Numerical simulation with linear high-order Boussinesq model is shown as the dashed lines. The convolution solution based on the non-uniform KdV approximation ζ_4 is shown as the full line in the top panel. The convolution solution based on the uniform approximation ζ_7 is shown as the full line in the bottom panel.

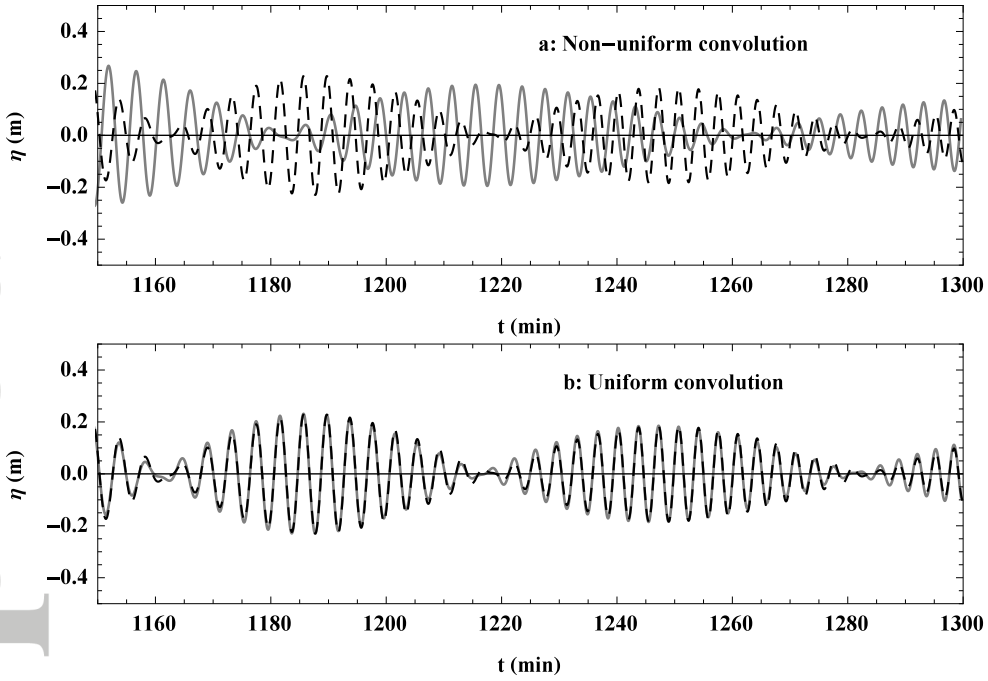

Figure 8. Second part of the time series of the surface elevation due to a monopole source. Description as in Figure 7.

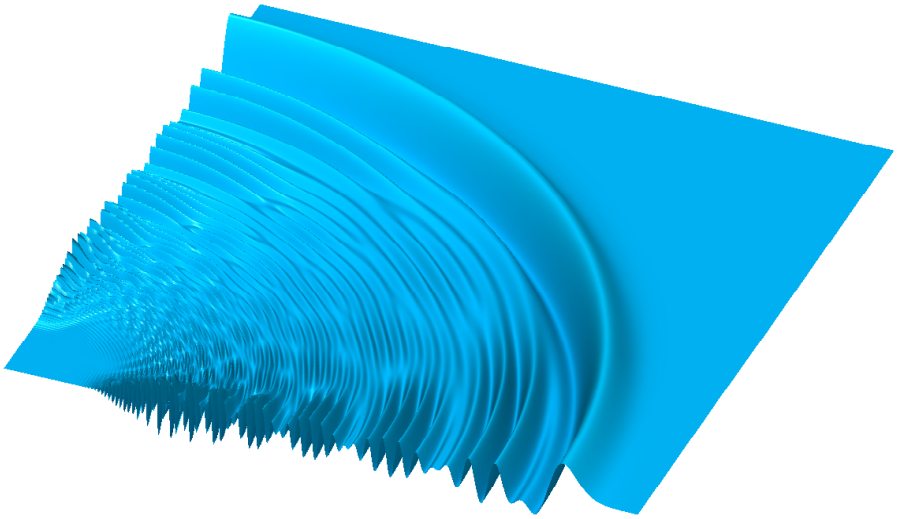

Figure 9. Snapshot of the surface elevation computed by the Boussinesq model for an initial square disturbance released at the lower left corner. Model dimensions are 2000 by 2000 grid points with a grid size of 1 km and a water depth of 4 km.

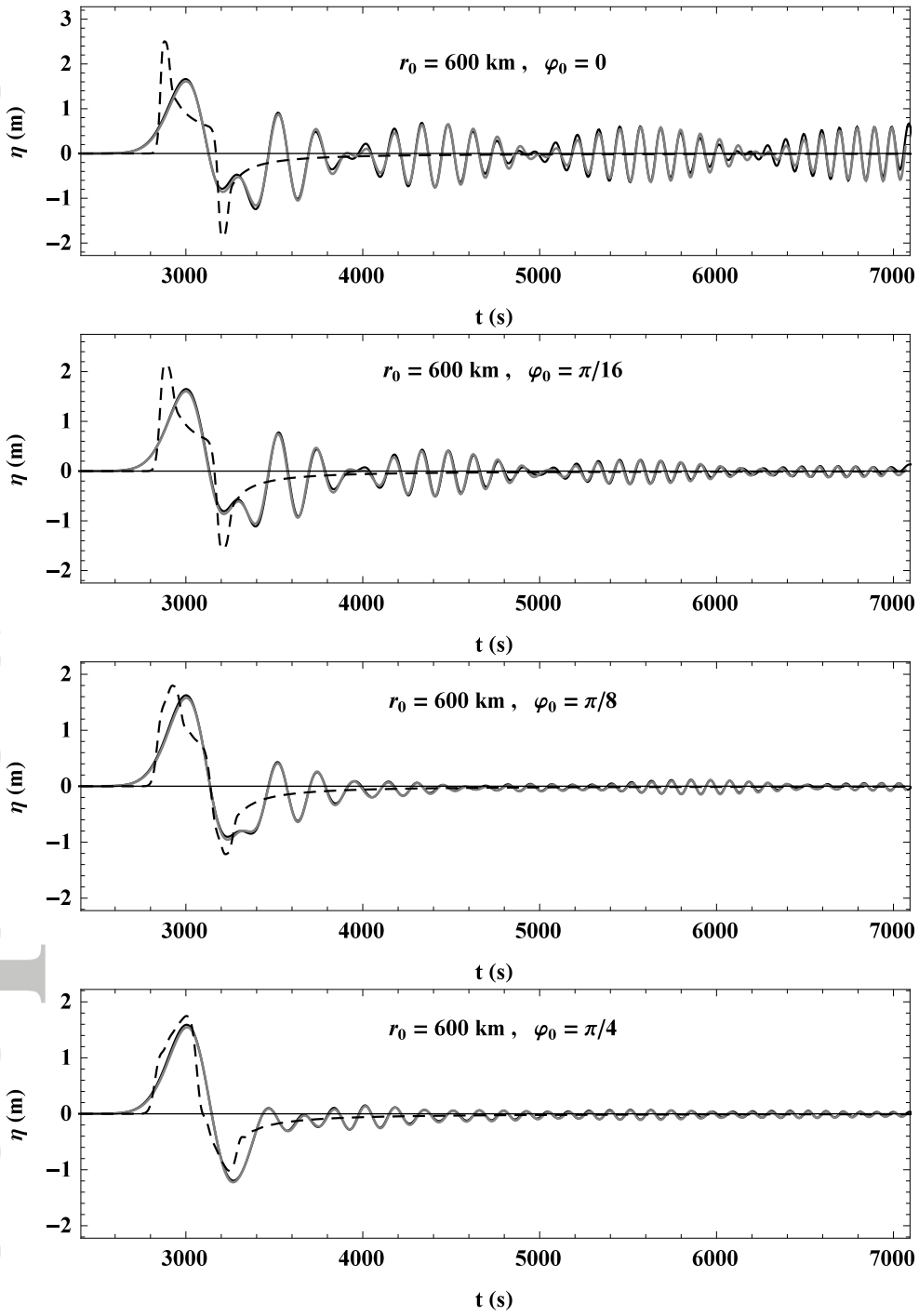

Figure 10a-d. Temporal variation of the surface elevation due to an initial square disturbance in 2D. Results obtained at the observation points defined by eq. (84). Gray line: The single convolution summation based on eq. (83); Black line: Results obtained by numerical simulation based on a Boussinesq model. Dashed line: Numerical simulation based on the linear shallow water equations.

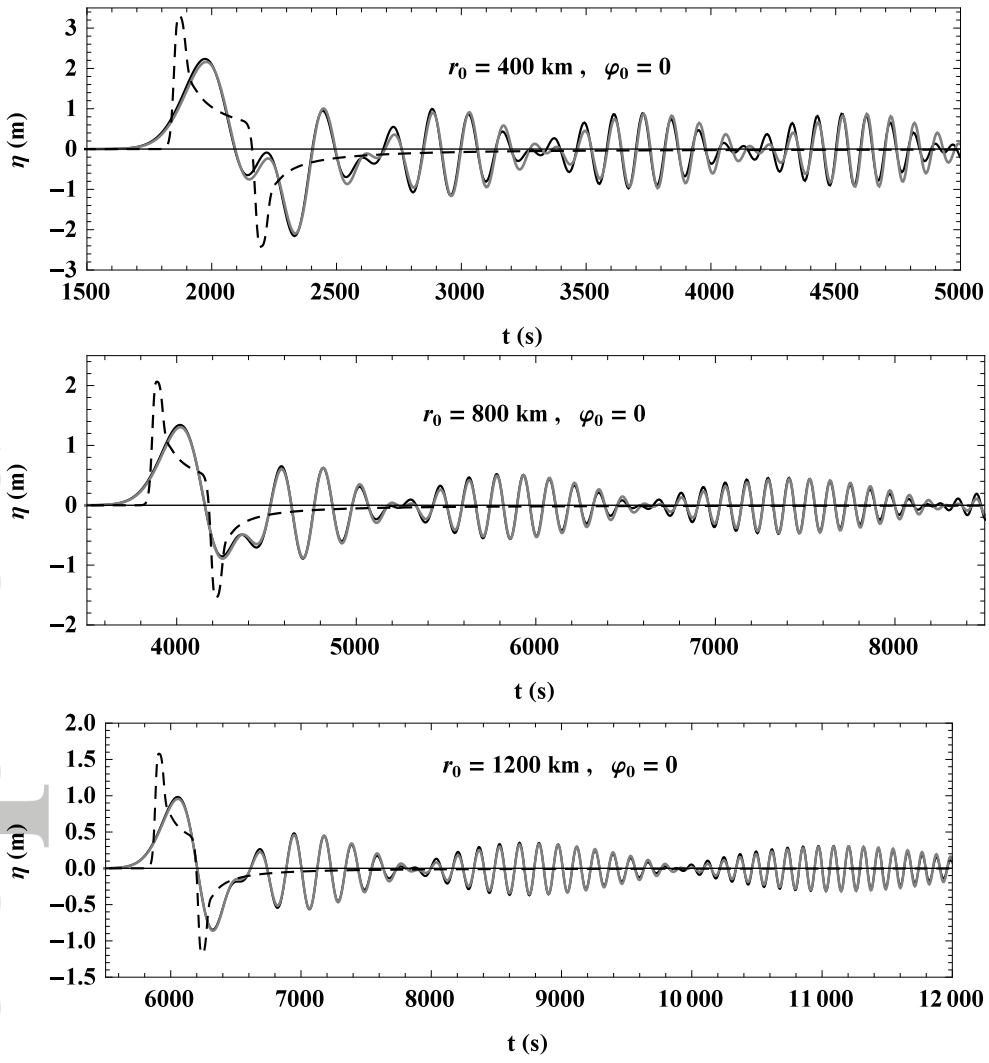

Figure 11a-c. Temporal variation of the surface elevation due to an initial square disturbance in 2D. Description as in Figure 10a-d.

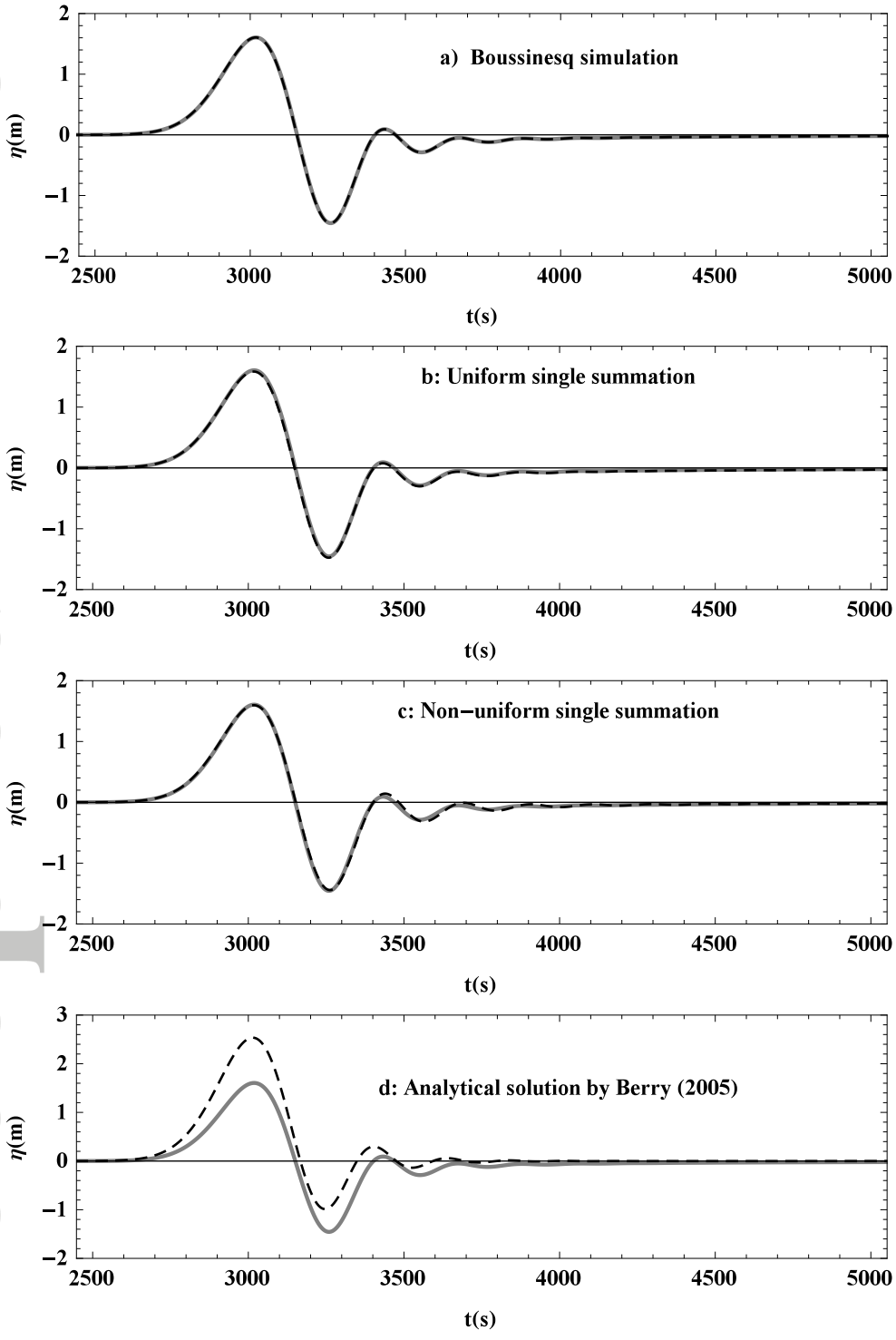

Figure 12a-d. Temporal variation of the surface elevation due to an initial Gaussian disturbance in 2D. Results are obtained at the location $r_0 = 600$ km from the center of the initial disturbance on a constant depth of $h = 4$ km. All panels show the direct integral solution as a full gray line. This is compared to the numerical Boussinesq simulation in panel a (black dashed); the uniform single summation convolution in panel b (black dashed); the corresponding non-uniform single summation convolution in panel c (black dashed); and the direct analytical solution in panel d (black dashed).

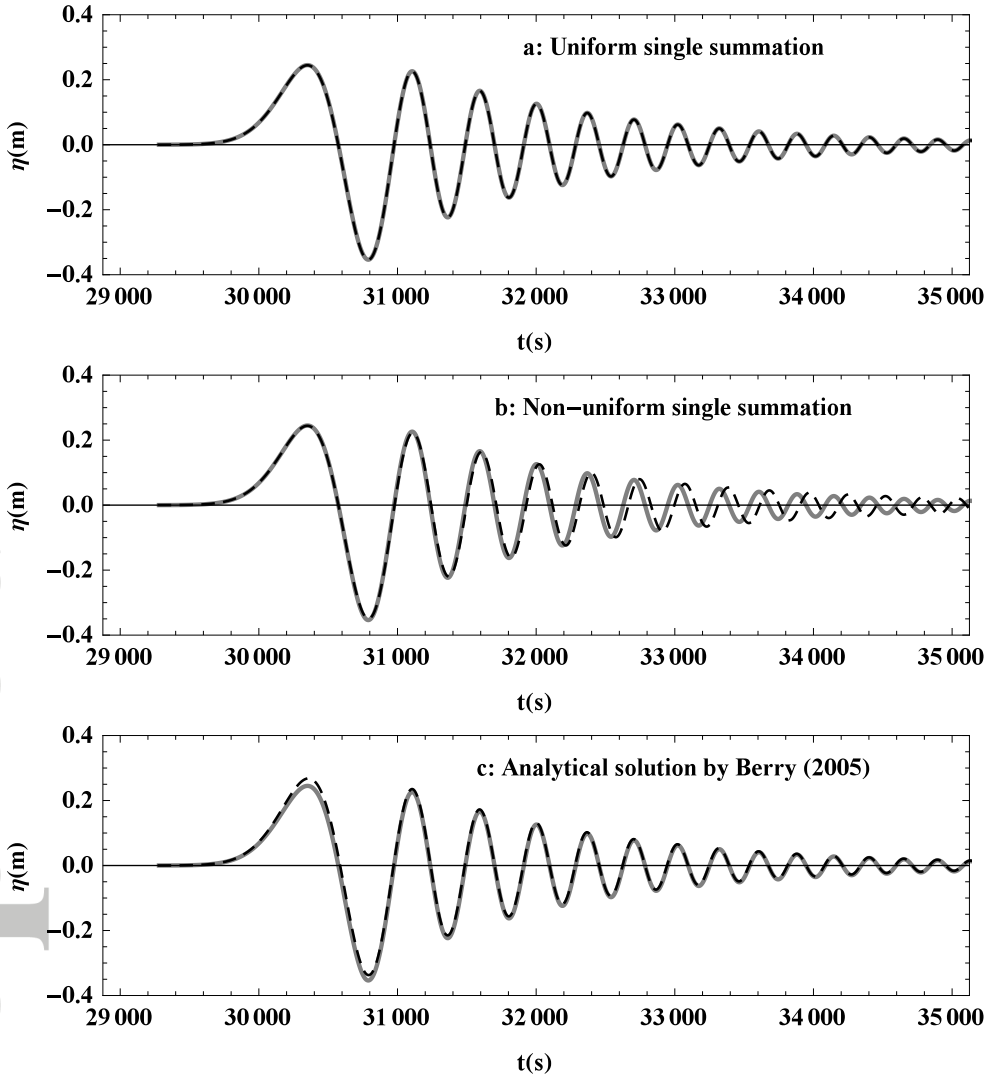

Figure 13a-c. Temporal variation of the surface elevation due to an initial Gaussian disturbance in 2D. Results are obtained at the location $r_0 = 6000$ km from the center of the initial disturbance on a constant depth of $h = 4$ km. All panels show the direct integral solution as a full gray line. This is compared to the uniform single summation convolution in panel a (black dashed); the corresponding non-uniform single summation convolution in panel b (black dashed); and the direct analytical solution in panel c (black dashed).

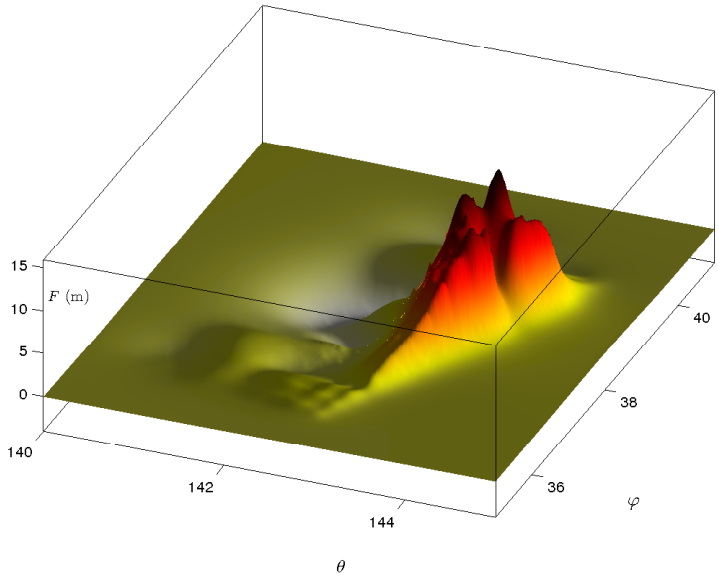

Figure 14. Perspective plot of the UCSB source from the 2011 Tohoku tsunami in Japan.

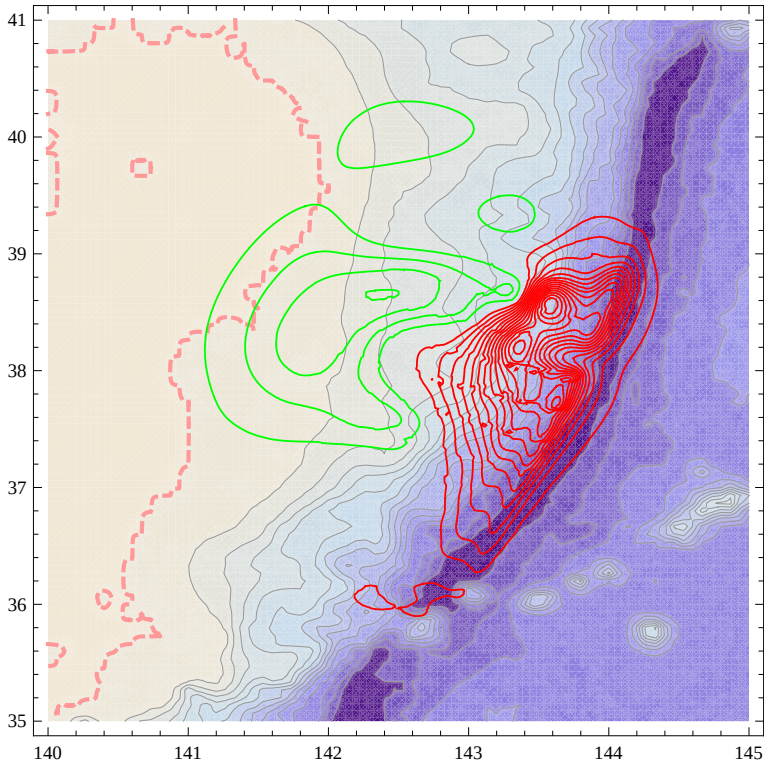

Figure 15. The local bathymetry with an overlay of contours from the UCSB source from the 2011 Tohoku tsunami in Japan. Positive/negative source values shown as red/green contours.

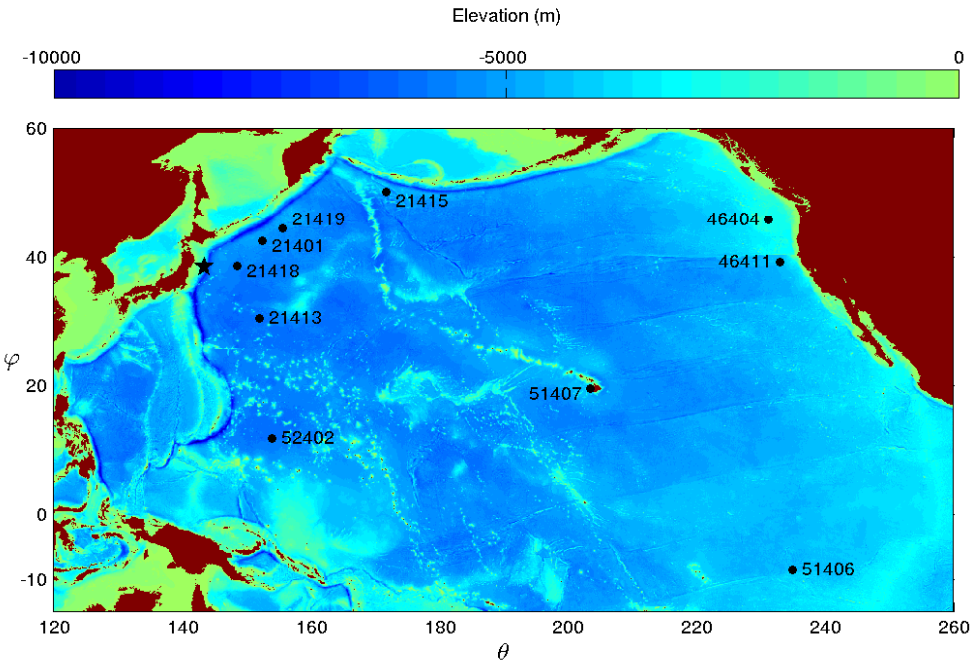

Figure 16. The Pacific including location of DART measurements. Source region indicated as a star.

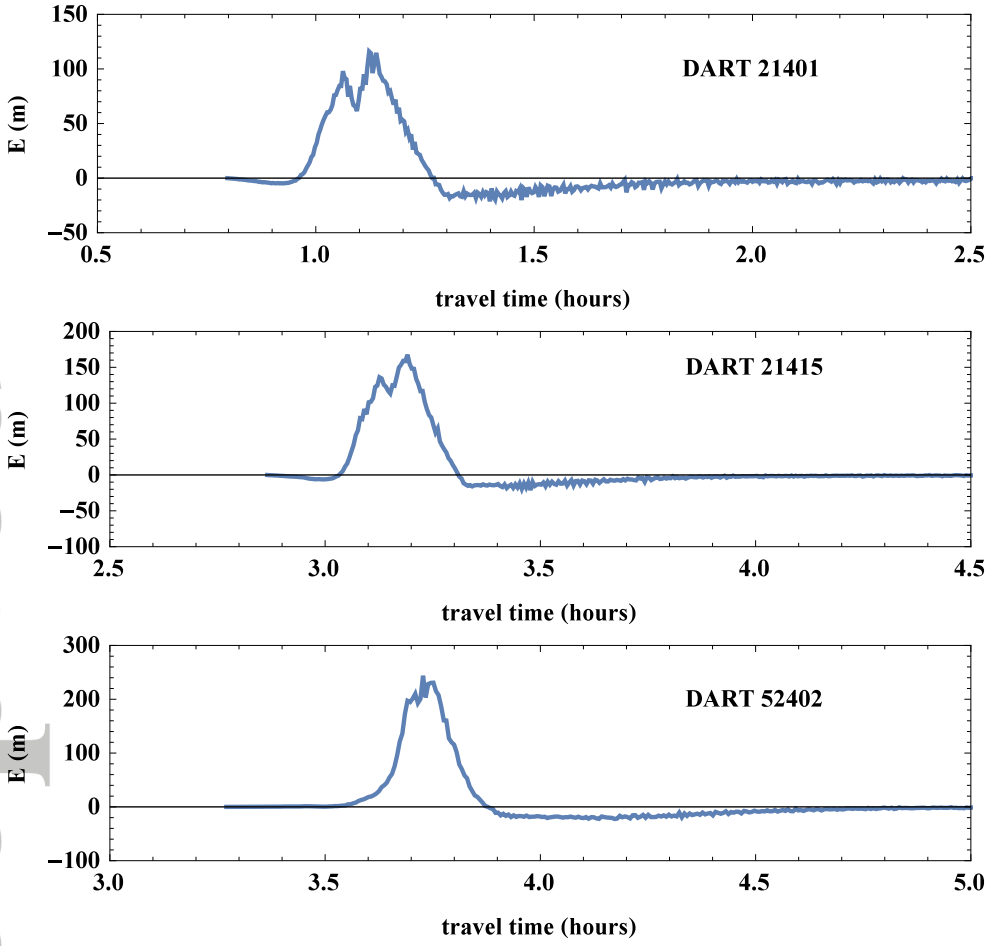

Figure 17. The accumulated source as a function of travel time for DART 21401, 21415 and 52402. E is determined by eq. (102).

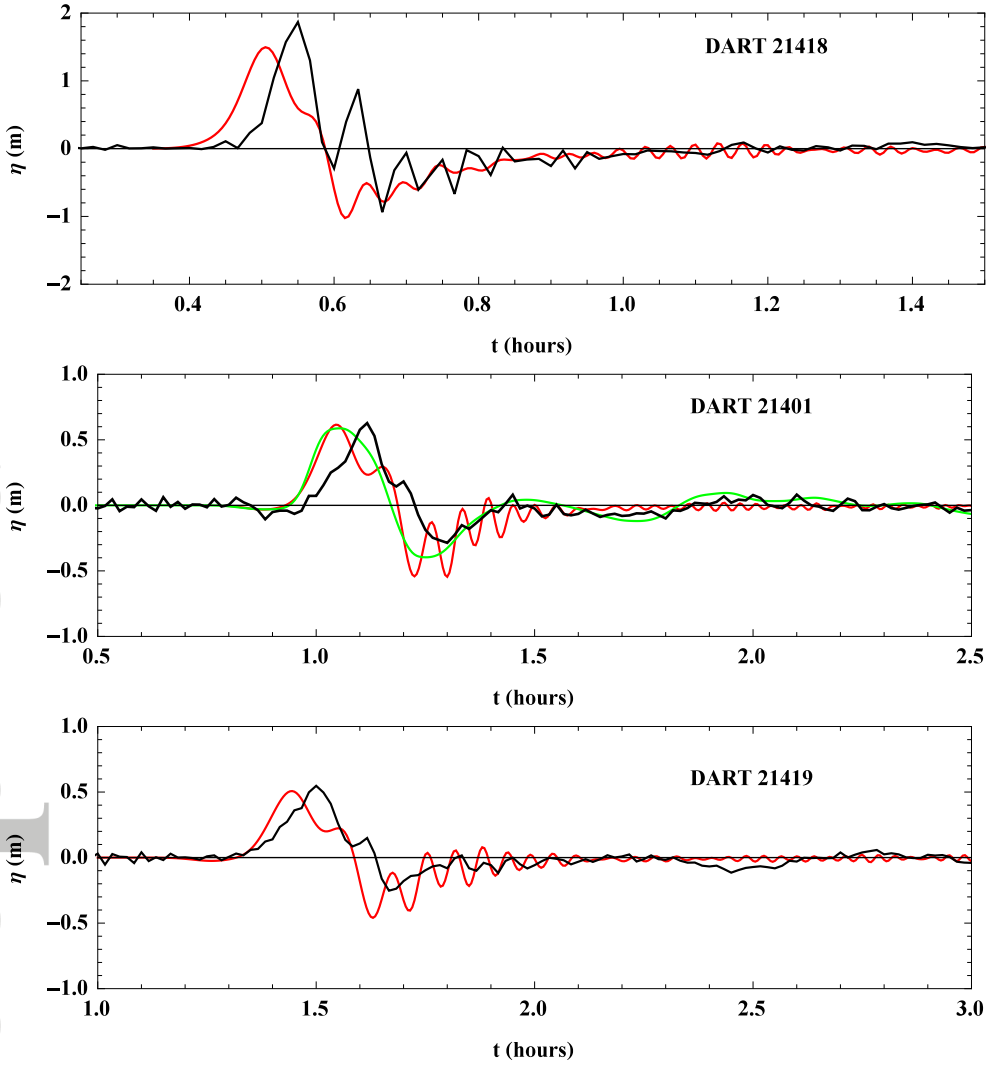

Figure 18a-c. Surface elevation at near-field DART buoys due to the 2011 Tohoku tsunami. Black: DART measurements; Red: Single summation convolution. Green: Numerical simulation based on the NSW equations.

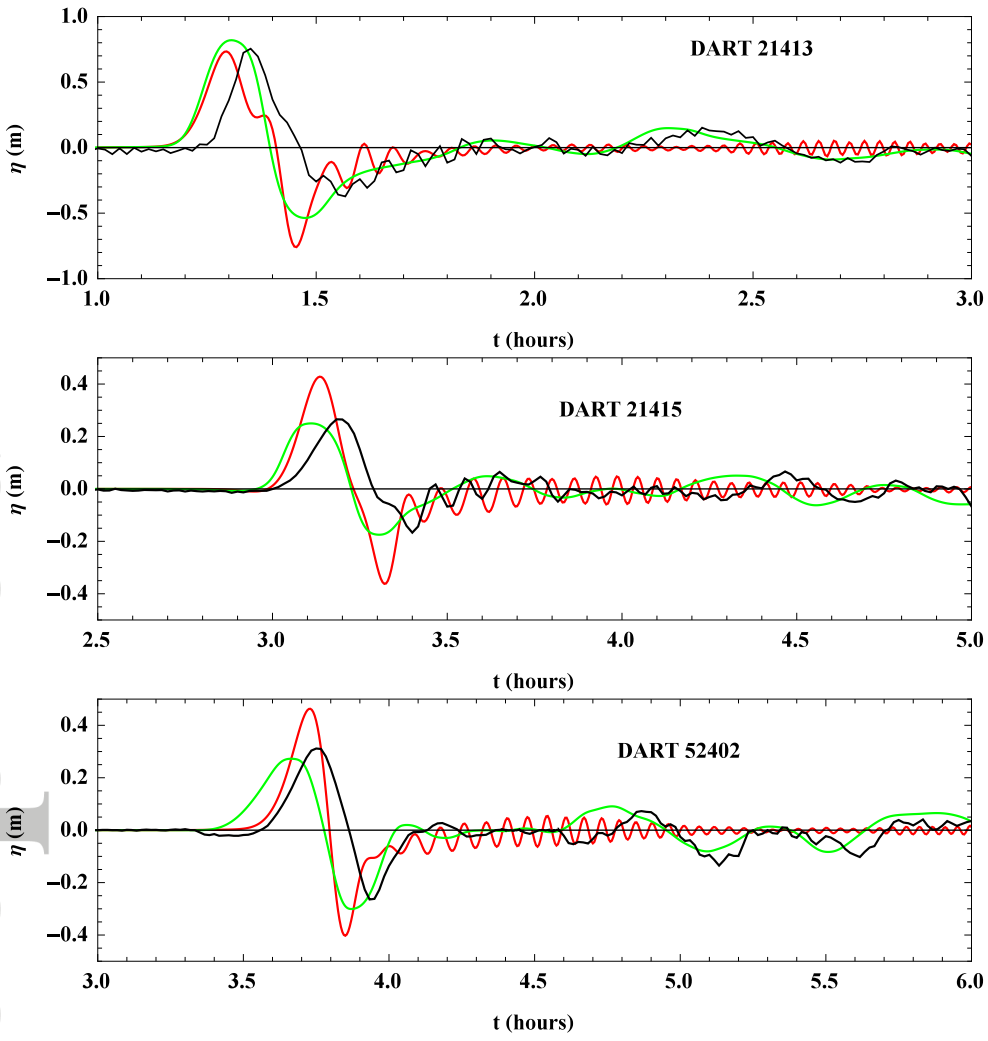

Figure 18d-f. Surface elevation at near-field DART buoys due to the 2011 Tohoku tsunami. Black: DART measurements; Red: Single summation convolution. Green: Numerical simulation based on the NSW equations.

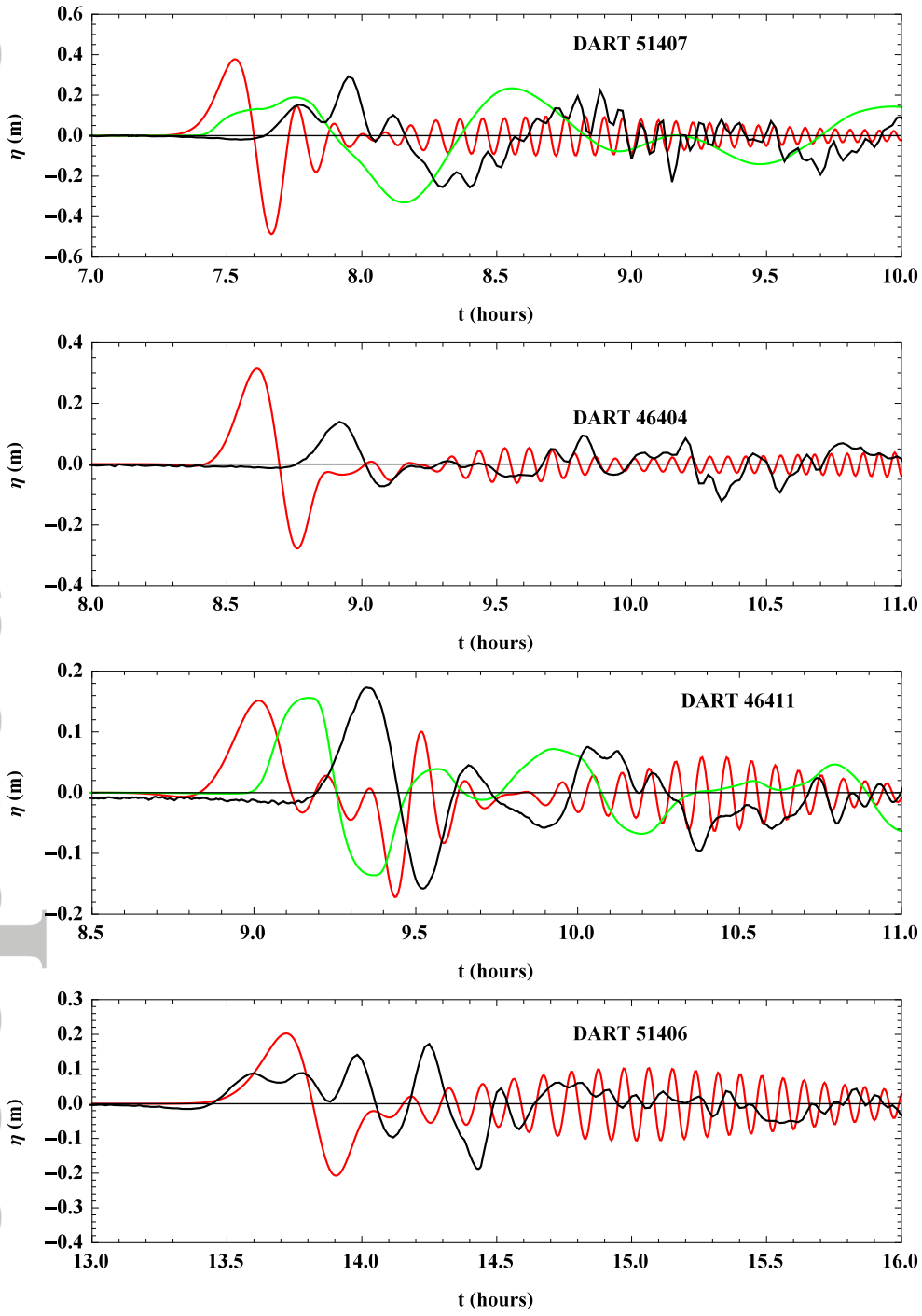

Figure 19a-d. Surface elevation at the far-field DART buoys due to the 2011 Tohoku tsunami. Black: DART measurements; Red: Single summation convolution. Green: Numerical simulation based on the NSW equations.